NTNU
Norwegian University of
Science and Technology

Development of a Long-Wave Infrared Laser Source Based on Optical Parametric Amplification in $ZnGeP_2$

Ingrid Anette Bakkland

Master of Science in Physics and Mathematics
Submission date: January 2016
Supervisor: Magnus Willum Haakestad, IFY

Norwegian University of Science and Technology
Department of Physics

Abstract

This thesis presents the design and implementation of an 8 μm laser source based on nonlinear conversion in $ZnGeP_2$. $ZnGeP_2$ is an attractive material for this purpose due to its high nonlinear coefficient, good transmission at the relevant wavelengths, and high thermal conductivity. The configuration was a master oscillator/power amplifier (MOPA) system, including an optical parametric oscillator (OPO) with a 3-mirror ring resonator that allows two passes of the beams through the same nonlinear crystal. The power amplifier consisted of two optical parametric amplifiers (OPAs). The MOPA system was pumped at 2.05 μm by a Q-switched Ho:YLF laser.

Each stage of the MOPA system was investigated with computational simulations to optimize the system for providing pulses at 8 μm wavelength with high energy and good beam quality. The experimental results were in good agreement with the simulations.

When pumping with 360 mJ, the maximum energy achieved at 8 μm was 45 mJ with $M^2 = 3.1$. The system was tested with different combinations of crystal lengths, and with both signal and idler as seeds, and only signal as seed in the power amplifier system. A conference paper describing the OPO has been accepted for presentation at Mid-Infrared Coherent Sources (MICS) [1].

Sammendrag

Denne masteroppgaven presenterer konstruksjonen og implementeringen av en 8 µm laserkilde basert på ulineær konvertering i $ZnGeP_2$. $ZnGeP_2$ har en høy ulineær koeffisient, god transmisjon for de relevante bølgelengdene og høy varmeledningsevne, noe som gjør det til et attraktivt materiale for dette formålet. Konfigurasjonen var et master oscillator/forsterker (MOPA)-system med en optisk parametrisk oscillator med en tre-speils ringresonator som tillater to passeringer av strålene gjennom den ulineære krystallen. Energiforsterkeren besto av to ulike optiske parametriske forsterkere (OPAer). MOPA systemet ble pumpet på 2.05 µm med en Ho:YLF laser.

Hvert steg av MOPA-systemet ble utforsket med numeriske simuleringer for å optimalisere systemet for å gi ut 8 µm pulser med høy energi og bra strålekvalitet. De eksperimentelle resulatene stemte bra med simuleringene.

Den maksimale energien på 8 µm som ble oppnådd med en pumpeenergi på 360 mJ, var 45 mJ med $M^2 = 3.1$. Systemet ble testet med ulike kombinasjoner av krystallengder, og med både idler og signal som input-stråler, og kun signal som input-stråle i forsterkningssystemet. En konferanseartikkel som beskriver OPOen har blitt akseptert for en presentasjon på 'Mid-Infrared Coherent Sources (MICS)' [1].

Preface

This thesis is the final part of a masters degree in Applied Physics at the Norwegian University of Science and Technology (NTNU). The degree includes a minimum of 300 credits, where 30 of these credits are from this thesis. The work I present was written in the period August 2015-January 2016, and the assignment was a continuation of a project that I performed during the summer 2015. The assignment was carried out at the Norwegian Defence Research Establishment (FFI), located at Kjeller.

I would like to thank my supervisor at FFI, Magnus W. Haakestad, for valuable guidance and advices during the work. Furthermore, I would also express my gratitude towards other members of the Electro-optics group at FFI from whom I have received help and suggestions.

Trondheim, 2016-01-22

Anette Bakkland

Contents

Chapter 1

Introduction

Coherent light sources emitting high-energy pulses with small spectral width in the mid-wave infrared (3-5 μm) and long-wave infrared (8-12 μm) have a tremendous number of applications including spectroscopy, remote sensing, surgery and defense against heat-seeking missiles [2]. One of the most important properties of a laser beam is how tightly it can be focused and how little it will spread in propagating to the far-field. This property is called 'beam quality' and is especially of great importance in terms of applications where you want to deliver as much as possible of the laser energy into a small aperture at a considerable distance. Laser wavelengths in applications that require good transmission in the atmosphere, are determined by regions where the atmosphere has low attenuation. In general, molecules in the atmosphere absorb photons at certain frequencies, leading to poor transmission of electromagnetic radiation. However, there are two distinct windows in the wavelength ranges 3–5 μm and 8–12 μm where the transmittance is high, as can be seen Fig. 1.1. For this reason, laser sources that operate in these wavelength ranges are of strong interest.

Most lasers have limited tuning range because the radiation originates from transitions between specific energy levels, leading to a lack of lasers that generate high energy beams in the 3-5 μm and 8–12 μm ranges directly. An alternative technique is nonlinear optical conversion of 1 μm or 2 μm laser sources. Optical parametric oscillators (OPOs) and optical parametric amplifiers (OPAs) constitute a class of frequency converting devices that are particularly interesting. Such devices can convert shorter wavelength light into two longer wavelengths through a non-

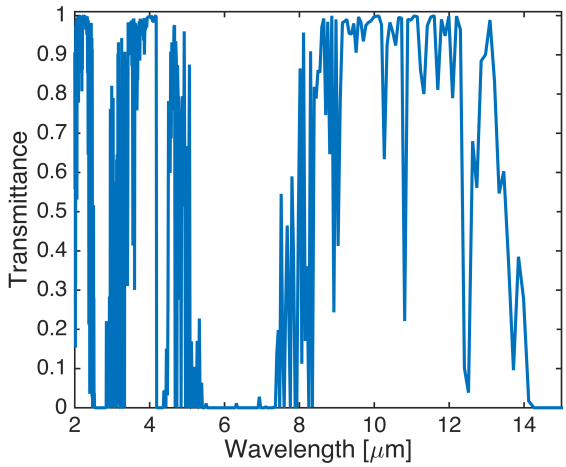

Figure 1.1: Atmospheric transmittance of radiation with an optical path length of 1 kilometer and a temperature of 23°C. Gas mixture: USA model, mean latitude, zero altitude, summer. The transmission is high in the wavelength ranges 3-5 µm and 8-12 µm which is commonly referred to as the atmospheric transparency windows. (Source: HITRAN)

linear three-wave mixing process. Emission can typically be tuned over hundreds of nanometers, giving selectable access to all wavelengths spanning from the ultraviolet to the long-wave infrared.

The field of nonlinear optics has developed rapidly since its beginning in 1961, shortly after the demonstration of the laser. In 1965, Giordmaine and Miller [3] built and demonstrated the first tunable optical parametric oscillator. Over the past decade, there has been remarkable progress in OPO device technology, driven by the emergence of new nonlinear materials and the availability of novel laser pump sources. The advent of birefringent crystals, as well as quasi-phase-matched nonlinear materials have had an exceptional impact on OPO technology and applications. Combined with the development of new solid-state, semiconductor and fiber laser pump sources, these have led to the practical realization of OPO devices with previously unattainable performance capabilities.

The most mature nonlinear materials suitable for implementing OPOs covering the 1-4.5 µm range are bulk and periodically poled ferroelectric oxides, including lithium niobate ($LiNbO_3$), potassium titanyl phosphate (KTP), potassium titanyl arsenate (KTA), or lithium tantalate ($LiTaO_3$).

Each of these materials can be pumped at 1 µm by use of solid-state lasers. Above 4.5 µm, standard oxide nonlinear materials exhibit strong bulk absorptions and are thus unsuitable. For wavelengths in the 8-12 µm range, it is thus required to use materials such as zinc germanium phosphide (ZGP), cadmium selenide (CdSe), silver thiogallate (AGS), silver selenogallate (AGSe), or gallium arsenide (GaAs) - that usually also require pump sources emitting above 2 µm [4].

In 2014, a highly efficient and high power mid-infrared (3-5 µm) source was produced by using nonlinear conversion of a 2.05 µm source in a ZGP crystal[5]. The 2.05 µm pump source was a high energy Ho:YLF laser [6]. ZGP crystals are attractive because of the high nonlinearity and good mechanical and thermal properties. ZGP is also commercially available in high quality. The ZGP transmission spectrum for wavelengths between 2-13 µm for a 10 mm crystal is shown in Fig. 1.2. It can be seen that the transmission is high for wavelengths between 2.0-8.3 µm.

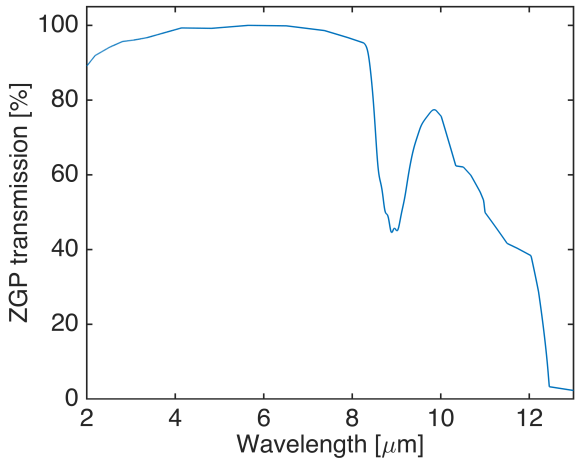

Figure 1.2: ZGP transmission for wavelengths between 2-13 µm. The measurements was performed at the Norwegian Defense Research Establishment (FFI).

Up to date, the highest energy obtained using nonlinear conversion in the 8–12 µm range is around 10 mJ [7, 8, 9]. The aim of this thesis has been to design and implement an 8 µm laser source with pulse energy of ~ 50 mJ and good beam quality based on nonlinear conversion in ZGP of a 2.05 µm pump source.

One of the greatest challenges in scaling nanosecond optical parametric oscillators to high energy is obtaining good beam quality along with high efficiency. This challenge is related to dam-

age threshold of optical components and the nonlinear crystal which limits the applicable optical intensities. In the context of laser-induced damage by laser pulses, the damage threshold of a material is often specified as the allowable peak fluence. The fluence of a laser pulse is the optical energy delivered per unit area (J/cm^2) and the peak fluence is the highest fluence value occurring within the laser beam profile. This means that for high energies in an OPO, the beam diameter needs to be increased to keep the peak fluence low, which can result in poor beam quality. This challenge will be addressed by using a *master oscillator/power amplifier* (MOPA) system. Such as system refers to a configuration consisting of one OPO, which provides the desired source wavelength, and one or several OPAs to amplify the energy. The MOPA in this assignment was implemented with a ZGP OPO which converted a low energy 2.05 µm pump beam into two beams at 2.76 µm (signal beam) and 8 µm (idler beam). Previous results have showed that seeding with both signal and idler in an OPA gives better conversion efficiency than seeding with signal only [5]. Both of the OPO output beams were therefore used as seeds in an ZGP OPA which was pumped by a 2.05 µm high energy beam. The first OPA stage was also tested with only the signal beam as seed. The amplified 2.76 µm from the first OPA stage was then used as pump in a second OPA stage where the 8 µm was further amplified.

Parametric processes such as parametric oscillation and amplification, require *phase matching* to be efficient. This means ensuring that a proper phase relationship between the interacting waves is maintained along the propagation direction. The phase matching can be of type I or type II. Type I phase matching means that the signal and idler have the same polarization, and type II phase matching means that the signal and idler have different polarization. Each stage of the system was investigated using a simulation tool with different types of phase matching to find the best combination. The simulation tool was also used to investigate parameters such as crystal lengths, beam diameters and resonator properties to optimize the MOPA system with the goal of making an output idler beam at 8 µm with highest possible energy and good beam quality.

This thesis will start with a chapter that serves the relevant theory for understanding nonlinear optical conversion. Chapter 3 presents the preliminary simulations that was performed in

order to optimize the experimental setup. The experimental procedure is explained in chapter 4, which includes the experimental setup and explanations of how the measurements were performed in the lab. Finally, chapter 5 presents the experimental results and discussion.

Chapter 2

Theory

In this chapter, the major equations relating to the performance of optical parametric devices are summarized. The nonlinear interactions in solids and the resultant coupling of electromagnetic waves that leads second order nonlinear processes will be described first. A more detailed description of difference-frequency generation (DFG), which is the involved nonlinear process in optical parametric amplification and oscillation, will then be given. The last section will be devoted to a discussion of the optical parametric oscillator and its performance parameters. Most of the content is based on the book 'Nonlinear Optics' by Boyd (2003) [10].

2.1 The Nonlinear Polarization

Optical phenomena that we observe in our every day life, e.g. refraction in a glass prism or the colors from the interference pattern of an oil film on water can to a very high degree of accuracy be describe by linear equations. In linear optics, the electromagnetic wave induces a polarization P in the dielectric material which is directly proportional to the applied electric field E and hence oscillates with the same frequency. However, if the electric field becomes sufficiently strong, the response of a material depends in a nonlinear manner and a full series expansion of the polarization in terms of successively higher orders of the electric field is needed. Typically, only laser light has sufficiently strong enough electric field to get a nonlinear response. The polarization of a nonlinear material is given by

$$P = \epsilon_o \chi^{(1)} E + \epsilon_0 \left(\chi^{(2)} E^2 + \chi^{(3)} E^3 + \cdots \right) = P^{\mathrm{L}} + P^{\mathrm{NL}}. \tag{2.1}$$

Here P^{L} denotes the linear part of the polarization, P^{NL} the nonlinear part and ϵ_0 is the electric permittivity of free space. The coefficients $\chi^{(n)}$ are the n-th order susceptibilities of the medium and the presence of such a term is generally referred to as an n-th order nonlinearity. For simplicity, the fields P and E are written as scalar quantities in Eq. 2.1. In the vector nature of the fields, $\chi^{(n)}$ is an $(n+1)$-order tensor representing both the polarization dependent nature of the parametric interaction as well as the symmetries of the nonlinear material.

For the relevance of the work in this thesis, we are primarily interested in effects that arise from the second-order nonlinearity $P^{(2)} = \epsilon_0 \chi^{(2)} E^2$. A simple order-of-magnitude estimate for when the second-order polarization would be comparable to the linear polarization, is when the applied electric field E is of the order of the characteristic atomic electric field strength $E_{\mathrm{at}} \approx 6 \cdot 10^{11}$ V/m. The second order susceptibility $\chi^{(2)}$ will then be of order $\chi^{(1)}/E_{\mathrm{at}}$. For condensed matter we have that $\chi^{(1)} \approx 1$, thus we expect that $\chi^{(2)} \approx 2$ pm/V.

The second-order nonlinear part is responsible for many interesting effects. Some examples of second-order processes are second harmonic generation (SHG), which occurs when light waves interact with themselves and create a polarization containing a component at the double original frequency. Sum-frequency generation (SFG) take place when the photon energies from the different fields are added and a photon with higher energy is created. Difference-frequency generation (DFG) occurs when the photons with lower energy are subtracted from the photons with higher energy. The latter is the underlying process of optical parametric amplification and oscillation.

The second-order nonlinear polarization arise from a $\chi^{(2)}$ nonlinearity which can occur only in noncentrosymmetric crystals, that is, in crystals that do not display inversion symmetry. The nonlinear polarization then has a spatial component P_i which depends quadratically on the electric field of an incident light wave. More precisely, the tensor nature of the nonlinear susceptibility needs to be considered and the second-order nonlinear term for the cartesian com-

ponent i can be written as

$$P_i(t) = \sum_{jk} \sum_{(nm)} 2 d_{ijk} E_j(\omega_n, t) E_k(\omega_m, t), \tag{2.2}$$

where the nonlinear tensor $d_{ijk} = \frac{1}{2}\chi^{(2)}_{ijk}$ has been introduced. The indices ijk refer to the cartesian components of the fields and (nm) refer to the summation over the harmonic components of frequencies n and m. Many tensor components can be zero for symmetry reasons, depending on the crystal class. For a fixed geometry, i.e. for fixed propagation and polarization directions, an effective value d_{eff} of the nonlinear tensor can be found for different crystal classes.

Consider the case of an electric field $E(t)$ that consists of two distinct frequency components, ω_1 and ω_2, and is incident upon a second-order nonlinear medium. The total incident electric field can then be written

$$E(t) = E(\omega_1) e^{-j\omega_1 t} + E(\omega_2) e^{-j\omega_2 t} + \text{c.c.}, \tag{2.3}$$

where $E(\omega_n) = A_n e^{jk_n z}$ for $n = 1, 2$. k_n is the wavenumber for the wave at frequency ω_n and is defined

$$k = \frac{n\omega}{c}, \qquad n = \sqrt{\epsilon^{(1)}(\omega)}, \tag{2.4}$$

where c is the speed of light in vacuum, n is the refractive index and $\epsilon^{(1)}$ is the relative permittivity of the material. n and $\epsilon^{(1)}$ are here written as scalar quantities which is valid if the material is isotropic. By using Eq. 2.2 the second-order nonlinear polarization is found to be

$$\begin{aligned}
P^{(2)}(t) =& 2 d_{eff}\left[|E(\omega_1)|^2 + |E(\omega_2)|^2\right], && \text{(dc-rectification)} \\
&+ 2 d_{eff} E(\omega_1) E(\omega_1) e^{-j(2\omega_1)t}, && \text{(SHG)} \\
&+ 2 d_{eff} E(\omega_2) E(\omega_2) e^{-j(2\omega_2)t}, && \text{(SHG)} \\
&+ 4 d_{eff} E(\omega_1) E(\omega_2) e^{-j(\omega_1+\omega_2)t}, && \text{(SFG)} \\
&+ 4 d_{eff} E(\omega_1) E^*(\omega_2) e^{-j(\omega_1-\omega_2)t}, && \text{(DFG)} \\
&+ \text{c.c.}
\end{aligned} \tag{2.5}$$

Eq. 2.5 shows that $P^{(2)}(t)$ contains components at five frequencies: 0, $2\omega_1$, $2\omega_2$, $\omega_1+\omega_2$ and $\omega_1-\omega_2$. The new generated frequency components are related to the processes dc-rectification, SHG, SFG and DFG, respectively. However, only one of the frequency components will typically be observable in the radiation generated by the nonlinear optical interaction. This is a consequence of that linear polarization only efficiently can produce an output signal if a certain phase-matching condition is satisfied (see section 2.3), and usually this condition can only be satisfied for one frequency component.

2.2 Difference-Frequency Generation

We have now seen how the response in a nonlinear material can cause the polarization to develop new frequency components not present in the incident field. These new frequency components of the polarization act as sources of new frequency components of the electromagnetic field. We will now consider the DFG process where the waves at frequencies ω_1 and ω_2 interact in a nonlinear medium to produce an output wave at the difference frequency $\omega_3 = \omega_1 - \omega_2$. This is a three-wave mixing process, which is a *parametric interaction*, that is, a process where the initial and final quantum-mechanical states of the system are identical. The nonlinear optical wave equation will be used as a starting point in the description of the new field components and we will see how the frequency components of the field become coupled by the nonlinear interaction.

The nonlinear optical wave equation can be derived from Maxwell's equations (p. 70 in [10]). If dissipation can be neglected, the nonlinear optical wave equation for an arbitrary isotropic material that is valid for each frequency component of the field can be written

$$\nabla^2\mathbf{E}_n - \frac{\epsilon^{(1)}(\omega_n)}{c^2}\frac{\partial^2\mathbf{E}_n}{\partial t^2} = \frac{1}{\epsilon_0 c^2}\frac{\partial^2\mathbf{P}_n^{\mathrm{NL}}}{\partial t^2}. \tag{2.6}$$

The equation has the form of a driven wave equation where the nonlinear response of the medium acts as a source term. In absence of a nonlinear source term, the solution for a plane

wave at frequency ω_n propagating in the z-direction is

$$E_n(z,t) = A_n e^{j(k_n z - \omega_n t)} + c.c., \tag{2.7}$$

where A_n is a *constant*. When the nonlinear source term is nonzero, but not too large, the solution to Eq. 2.6 will still be on the form of Eq. 2.7, except that A_n will become a slowly varying function of z.

The polarization field appearing in Eq. 2.6 can be represented on the form

$$P_n(z,t) = P_n e^{-j\omega_n t} + c.c. \tag{2.8}$$

The amplitudes P_n of the second order nonlinear polarization components at the three frequencies ω_1, ω_2 and ω_3 can be found from Eq. 2.5 and are given by

$$P_1 = 4 d_{eff} A_2 A_3 e^{j(k_2+k_3)z}, \tag{2.9a}$$

$$P_2 = 4 d_{eff} A_1 A_3^* e^{j(k_1-k_3)z}, \tag{2.9b}$$

$$P_3 = 4 d_{eff} A_1 A_2^* e^{j(k_1-k_2)z}. \tag{2.9c}$$

Here, P_1 is related to a SFG process and P_2 and P_3 to DFG processes. By substituting Eqs. 2.7 and 2.9 into the wave equation 2.6, and assuming that

$$\left| \frac{d^2 A_n}{dz^2} \right| \ll \left| k_n \frac{dA_n}{dz} \right|, \tag{2.10}$$

the equations that describe the evolution of the slowly varying complex amplitudes of the three waves can be obtained as

$$\frac{dA_1}{dz} = \frac{2j\omega_1}{n_1 c} d_{eff} A_2 A_3 e^{-j\Delta kz}, \tag{2.11a}$$

$$\frac{dA_2}{dz} = \frac{2j\omega_2}{n_2 c} d_{eff} A_1 A_3^* e^{j\Delta kz}, \tag{2.11b}$$

$$\frac{dA_3}{dz} = \frac{2j\omega_3}{n_3 c} d_{eff} A_1 A_2^* e^{j\Delta kz}, \tag{2.11c}$$

where $\Delta k = k_1 - k_2 - k_3$ is the wave vector mismatch. The intensity associated with each wave is given by

$$I_n = 2 n_n \epsilon_0 c |A_n|^2, \tag{2.12}$$

and the corresponding photon flux is $F_n = I_n / \hbar\omega_n$, where $\hbar$ is the reduced Planck constant. By considering the intensity and the photon flux, a useful conservation law can be obtained from Eqs. 2.11. By multiplying both sides of Eq. 2.11a by A_1^* and both sides of Eq. 2.11b by A_2^*, and similarly for Eqs. 2.11b and 2.11c, we arrive at the following relation:

$$-\frac{dF_1}{dz} = \frac{dF_2}{dz} = \frac{dF_3}{dz}. \tag{2.13}$$

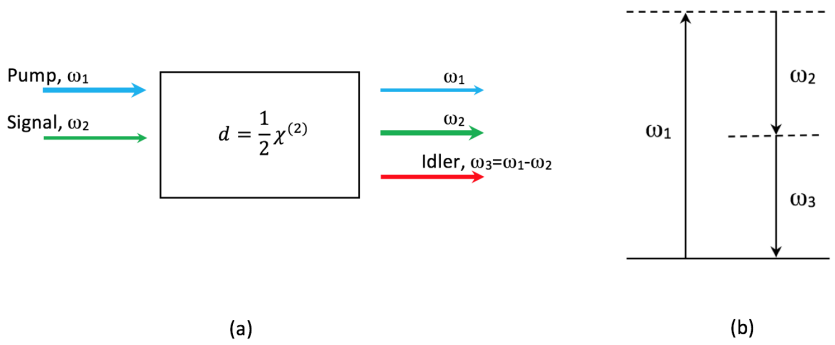

Figure 2.1: Difference-frequency generation. (a) Geometry of the interactions in the nonlinear material. (b) Energy-level diagram.

Eq. 2.13 can then be related to a photon interaction, where the number of photons must be conserved. The three-photon interaction is illustrated in Fig. 2.1. It can be seen that conservation of energy requires that for every photon that is created at the difference frequency ω_3, a photon

at ω_1 must be destroyed and a photon at ω_2 must be created.

If we now assume that the wave at ω_1 is unaffected by the interactions, the amplitude A_1 can be treated as a constant. For the case of perfect phase matching, $\Delta k = 0$, and assuming the boundary conditions

$$A_3(0) = 0, \qquad A_2(0) = \text{arbitrary}, \tag{2.14}$$

the solutions for A_2 and A_3 are

$$A_2(z) = A_2(0)\cosh\kappa z, \tag{2.15a}$$

$$A_3(z) = j\left(\frac{n_2\omega_3}{n_3\omega_2}\right)^{1/2}\frac{A_1}{|A_1|}A_2^*(0)\sinh\kappa z, \tag{2.15b}$$

where κ is a coupling constant defined as

$$\kappa = \frac{2d_{eff}\omega_2\omega_3}{\sqrt{k_2k_3}c^2}|A_1|. \tag{2.16}$$

Eq. 2.15a and 2.15b shows that both fields experience monotonic and asymptotic growth. The ω_2 wave retains its initial phase and is simply amplified by the interaction, while the generated ω_3 wave has a phase that depends on both the ω_1 and ω_2 wave.

If we now consider the situation where $\Delta k \neq 0$, both waves at ω_1 and at ω_2 are unaffected by the interaction, and the wave at ω_3 have the boundary condition $A_3(0) = 0$, the solution for A_3 can simply be found by integrating Eq. 2.11c:

$$A_3(z) = \frac{2\omega_3}{n_3c}\frac{d_{eff}}{\Delta k}A_1A_2^*(e^{j\Delta kz} - 1). \tag{2.17}$$

The intensity of this wave will be proportional with the factor $\text{sinc}^2(\Delta kz/2)$, which is plotted in Fig. 2.2. It can be seen that the intensity is maximum when the condition

$$\Delta k = k_p - k_s - k_i = 0 \tag{2.18}$$

is fulfilled. Eq. 2.18 is the condition for perfect phase matching. When this condition is fulfilled, the generated wave maintains a fixed phase relation with respect to the nonlinear polarization and is able to extract energy most efficiently from the incident waves. When $\Delta k \neq 0$, the intensity of the emitted radiation is smaller. The distance over which this function goes to zero is defined as the coherence length and is given by

$$L_c = \frac{2\pi}{\Delta k}. \tag{2.19}$$

At this length, the fields have accumulated a phase shift of 2π between each other and the energy will start to flow in the opposite direction.

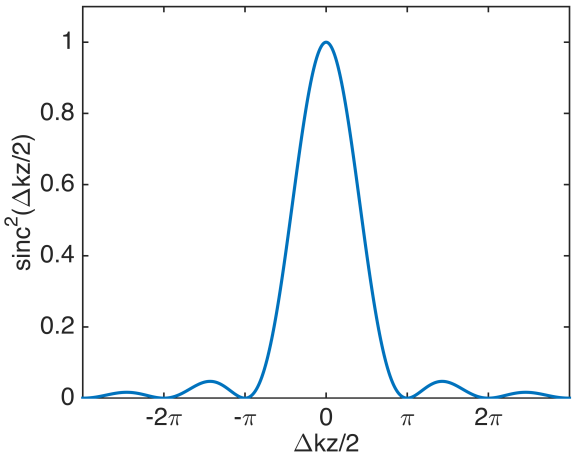

Figure 2.2: Effects of the wave vector mismatch Δk on the intensity of the generated wave in the DFG process.

A numerical solution to the coupled-amplitude equations 2.11 for the general case can be seen in Fig. 2.3, where (a) shows the case where $\Delta k = 0$ and (b) shows the case where $\Delta k = 1$ mm^{-1}. The initial conditions was $I_1(0) = 0.24$ GW/cm^2, $I_2(0) = 0.007$ GW/cm^2 and $I_3(0) = 0$, and the waves had wavelengths $\lambda_1 = 2.05$ µm, $\lambda_2 = 2.76$ µm and $\lambda_3 = 8.00$ µm. It can be seen that the intensity is periodically converted between the waves when they propagate through the nonlinear medium. When $\Delta k = 0$, complete conversion is obtainable at certain lengths within the medium, but when Δk is nonzero, it can be seen that the conversion process is less efficient. The total intensity is constant at all lengths in both cases, which agrees with the conservation law in

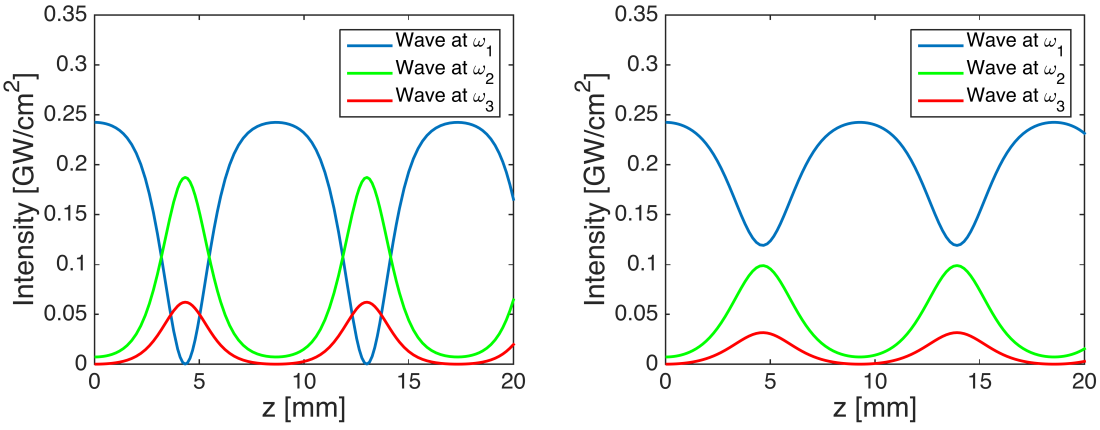

(a) (b)

Figure 2.3: Evolution of the intensity of three interacting waves in a nonlinear crystal with a length of 20 mm. $\Delta k = 0$ in (a) and $\Delta k = 1$ mm^{-1} in (b). The input waves at ω_1 and ω_2 have intensities $I_1 = 0.24$ GW/cm^2 and $I_2 = 0.007$ GW/cm^2 on the crystal entrance, and periodically generate a new wave at ω_3 while propagating through the crystal.

Eq. 2.13. Ideal conversion occurs when the waves at ω_2 and ω_3 reaches maximum intensity. After this point, the energy flow in the process changes direction, and the energy of the waves at ω_2 and ω_3 is converted back to the ω_1 wave. This effect is called back-conversion. Choosing a nonlinear crystal with a length that minimizes back-conversion is therefore an important factor when implementing nonlinear conversion devices. It should also be noticed that the oscillation of the periodical conversion is more rapid when $\Delta k = 0$.

Because DFG is an amplification process, it is also known as optical parametric amplification. If the nonlinear medium is placed inside an optical resonator, the ω_2 and/or ω_3 fields can build up to large values. Such a device is known as an optical parametric oscillator (OPO). From now on, the waves at frequency ω_1, ω_2 and ω_3 will be referred to as *pump*, *signal* and *idler*, respectively, with the subscripts p, s and i.

2.3 Phase-Matching (collinear propagation)

The effect of wave vector mismatch is included entirely in the factor $\text{sinc}^2(\Delta kL/2)$, which is plotted in Fig. 2.2. The condition $\Delta k = k_1 - k_2 - k_3 = 0$ which gives the maximum efficiency in the conversion process is called the *phase matching condition*. For convenience, the condition can

be rewritten as

$$\frac{n_p}{\lambda_p} = \frac{n_s}{\lambda_s} + \frac{n_i}{\lambda_i}. \tag{2.20}$$

If the mixed three waves are collinear and the the medium is non-dispersive, the phase matching condition is automatically satisfied if $\omega_p = \omega_s + \omega_i$. However, all materials are in reality dispersive, and n_p, n_s and n_i will be different. As a consequence, in isotropic media with normal dispersion, the condition in Eqs. 2.20 and the frequency-matching condition $\omega_p = \omega_s + \omega_i$ can not usually be simultaniously satisfied because the refractive index is an increasing function of frequency. A common procedure for achieving phase matching is to make use of anisotropic media. In such a material the optical response is directional dependent and the refractive index $n(\omega)$ is a 3x3 tensor. If the coordinate system used coincides with the principal axes of the crystal, the non-diagonal elements are zero. Furthermore, if two of the elements (n_x and n_y) are equal, the crystal is called uniaxial. The z-direction is called the optic axis and the refractive index in this direction is called the extraordinary index n_e. The refractive index in the x- and y-directions are the ordinary index n_o. The *birefringence* of the material is the difference between these indices of refraction, $\Delta n = n_e - n_o$. $\Delta n > 0$ and $\Delta n < 0$ is denoted a positive or negative uniaxal crystal, respectively.

2.3.1 Angle tuning

In practice, the nonlinear medium used in OPA and OPO devices is often a uniaxial crystal. By selection of polarization, each of the three waves can be ordinary or extraordinary. For an ordinary wave, $n(\omega) = n_o(\omega)$ and for an extraordinary wave, $n(\omega) = n_e(\theta, \omega)$. The refractive index of the extraordinary wave depends on the angle θ between the direction of the wave and the optical axis of the crystal in accordance with the relation

$$\frac{1}{n_e^2(\theta,\omega)} = \frac{\sin^2\theta}{n_e^2(\omega)} + \frac{\cos^2\theta}{n_o^2(\omega)}. \tag{2.21}$$

This phenomena is represented graphically by an index ellipsoid in Fig. 2.4. Note that $n_e(\theta,\omega)$ is equal to the principal value $n_e(\omega)$ for $\theta = 90°$ and is equal to $n_o(\omega)$ for $\theta = 0°$. Phase matching is

achieved by adjusting the angle θ to achieve the value of $n_e(\theta,\omega)$ for which the phase matching condition is satisfied. This technique is called *angle tuning*.

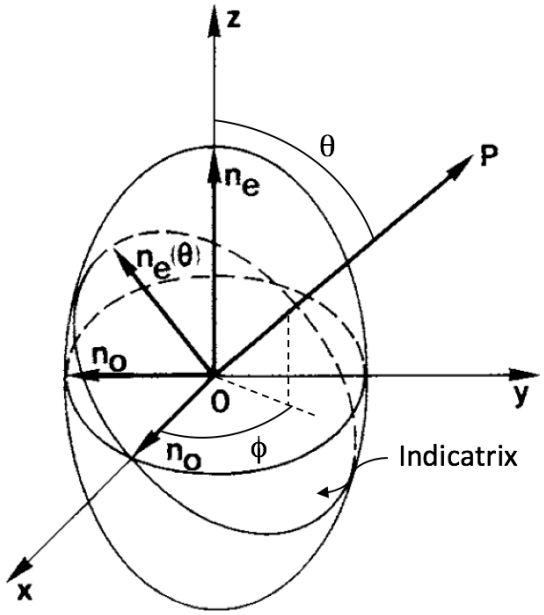

Figure 2.4: The index ellipsoid for a positiv uniaxial crystal. The coordinates (x,y,z) are the principal axes and the optical axis is in the z-direction. The indicatrix is formed by the plane through O, perpendicular to the propagation direction **P**. The direction of the two axes of the indicatrix gives the polarization directions, and the length of the semi axes gives the corresponding refractive index.

There are two two choices for the polarizations of the lower-frequency waves. If the polarizations of the signal and idler waves are the same, the wave mixing is said to be **Type I**; if they are orthogonal, it is said to be **Type II**. The possibilities are summarized in Table 2.1.

Table 2.1: Phase-matching conditions for uniaxial crystals.

	Positive uniaxial	Negative uniaxial
Type I	$n_p^o/\lambda_p = n_s^e(\theta)/\lambda_s + n_i^e(\theta)/\lambda_i$	$n_p^e(\theta)/\lambda_p = n_s^o/\lambda_s + n_i^o/\lambda_i$
Type II	$n_p^o/\lambda_p = n_s^e(\theta)/\lambda_s + n_i^o/\lambda_i$	$n_p^e(\theta)/\lambda_p = n_s^o/\lambda_s + n_i^e(\theta)/\lambda_i$

It should be emphasized that phase matching is not possible in all uniaxial crystals. Favorable optical properties of a particular crystal are large birefringence and small dispersion [11]. The

strength of the output signal is also dependent of the angle ϕ of the phase matched direction. The effective nonlinear coefficient d_{eff} is a function of ϕ, and often one can choose ϕ such that the value of d_{eff} is maximized.

2.3.2 Phase matching bandwidth

The phase matching bandwidth is defined as the width of an optical frequency range in which the nonlinear interaction process can be efficient due to more or less precise phase matching. If we assume that the pump frequency bandwidth is zero, $\Delta\omega_p = 0$, it follows that $\Delta\omega_s = -\Delta\omega_i$. The wave vector mismatch $\Delta k = k_p - k_s - k_i = (n_p\omega_p - n_s\omega_s - n_i\omega_i)/c$ then varies according to

$$d(\Delta k) = \frac{\partial \Delta k}{\partial \omega_s} d\omega_s + \frac{\partial \Delta k}{\partial \omega_i} d\omega_i = \left(\frac{\partial \Delta k}{\partial \omega_s} - \frac{\partial \Delta k}{\partial \omega_i}\right) d\omega_s = \frac{1}{c}\left(n_i + \omega_i \frac{\partial n_i}{\partial \omega_i} - n_s - \omega_s \frac{\partial n_s}{\partial \omega_s}\right) d\omega_s. \quad (2.22)$$

By introducing the group velocity

$$v_g = \frac{c}{n(\omega) + \omega \frac{\partial n}{\partial \omega}}, \quad (2.23)$$

Eq. 2.22 can be rewritten as

$$d(\Delta k) = \left(\frac{1}{v_{g,i}} - \frac{1}{v_{g,s}}\right) d\omega_s. \quad (2.24)$$

This shows that phase matching bandwidth is related to group velocity mismatch. The propagation time over a length L is L/v_g, so a variation in group velocities leads to temporal separation of pulses with different polarization of frequency. This phenomena is called *temporal walk-off*. As explained in Section 2.2, Δk must be small to achieve an efficient conversion process. A common condition for an acceptable phase mismatch is when the intensity is half of its maximum value, i.e. when $\Delta k L/2 = \pm 1.39$ (see Fig. 2.2), where L is the crystal length. The condition that needs to be satisfied for three collinear beams can then be written

$$|\Delta k \cdot L| < 2.78. \quad (2.25)$$

The phase matching bandwidth of the signal and idler waves can then simply be written

$$\Delta\omega_s = \Delta\omega_i = \frac{5.56}{\left|\frac{1}{v_{g,i}} - \frac{1}{v_{g,s}}\right| L}. \tag{2.26}$$

Note that the phase matching bandwidth usually is wider for type I phase matching than for type II phase matching because the difference in group velocity of the signal and idler is usually bigger if the beams have different polarization. For type II phase matching, the $\Delta\omega_s$ will always be finite, while for type I phase matching, $\Delta\omega_s$ is infinite at degeneracy. By combining the relations $\Delta\omega/\omega = -\Delta\lambda/\lambda$ and $\omega = 2\pi c/\lambda$, the bandwidth in terms of wavelength is found to be

$$\Delta\lambda = \frac{\lambda^2 \Delta\omega}{2\pi c}. \tag{2.27}$$

From this relation it can be seen that even though the signal and idler frequency bandwidth are equal, the wavelength bandwidths are different at nondegenerate frequencies. For a parametric mixing in a ZGP crystal with L = 10mm with type II phase matching with a 2.76 µm signal wave with extraordinary polarization and an 8 µm idler wave with ordinary polarization, the acceptance bandwidths will be 13.3 nm and 111.6 nm, respectively.

2.3.3 Spatial walk-off

For a laser beam propagating in an isotropic medium, the transverse intensity distribution propagates along the beam propagation direction. Mathematically this means that the Poynting vector $\mathbf{S} = \mathbf{E} \times \mathbf{H}$ which represents the directional energy flux density of an electromagnetic wave is parallel with the wave vector $\mathbf{k}$. However, in a birefringent medium, the intensity distribution can drift away from the direction defined by the wave vector. This phenomenon is called spatial walk-off and is associated with the angle ρ between $\mathbf{S}$ and $\mathbf{k}$. The walk-off angle can be calculated from the equation [12]

$$\rho = -\frac{1}{n_e}\frac{dn_e}{d\theta}. \tag{2.28}$$

Spatial walk-off occurs only for beams with extraordinary polarization, where the polarization is not parallel to a crystal axis. The minus sign in Eq. 2.28 indicates that the walk-off occurs in

the direction where the refractive index would decrease. If the beams interacting in a nonlinear crystal have different polarizations, their walk-off angles are also different and the beams intensity distribution will walk away from each other as they propagate through the crystal. A consequence is that the interaction length and thus the conversion efficiency can be limited, and the beam profiles can be distorted.

The problem of walk-off can be reduced by using two crystals which are oriented such that the walk-off directions are opposite to each other. The crystals can for instance be orientated such that the beams will walk away from each other in the first crystal and towards each other in the second crystal. The overall walk-off effect can then be strongly reduced.

For a ZGP crystal with type II phase matching with a 2.76 µm signal wave and an 8 µm idler wave, the walk-off angle of the extraordinary signal wave is 0.53°. For a 10 mm long crystal and beam diameters of 2.3 mm, this walk-off angle corresponds to a displacement of less than 5% of the beam diameter. One can therefore conclude that for this particular interaction, spatial walk-off will not have an appreciable effect.

2.3.4 Acceptance angles

Acceptance angles give information about tolerance to misaligned crystals, misaligned beams or divergent beams. In real devices the divergence of beams as well as the experimental setup set limits for achieving perfect collinear beams. In the case of non-collinear beams, the phase mismatch is

$$\Delta\mathbf{k} = \mathbf{k}_p - \mathbf{k}_s - \mathbf{k}_i. \tag{2.29}$$

This means that both the phase mismatch in the transverse direction, $\Delta k_\perp$, and in the longitudinal direction, Δk_z, must be zero to achieve perfect phase matching. In many devices where there are one or two input beams, the remaining beams can adapt their direction to cancel the transverse part of the phase mismatch, such that $\Delta k_\perp = 0$.

If the pump beam has a fixed direction along the z axis, the acceptance angle interval can in this

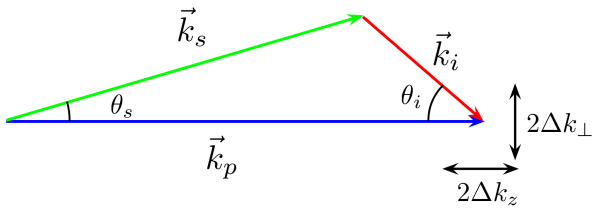

Figure 2.5: Three-wave interaction with non-collinear beams.

case be derived in the same manner as the frequency acceptance interval, with the condition $|\Delta k_z|L \leq 2.78$. The acceptance angle $\Delta\theta_s$ for the signal, can then be written

$$\Delta\theta_s = \frac{5.56}{\left|\frac{\partial k_{s,z}}{\partial\theta_s} - \frac{k_s}{k_i}\frac{\partial k_{i,z}}{\partial\theta_i}\right| L}. \tag{2.30}$$

Note that $\Delta\theta_s \neq \Delta\theta_i$ because of the factor k_i/k_s. If only the signal wave has extraordinary polarization, $\frac{\partial k_{i,z}}{\partial\theta_i} = 0$. The signal acceptance angle $\Delta\theta_s$ is then analogous with the acceptance angle for misaligning the direction of the crystal.

If the nonlinear device has three input beams, all beams have fixed directions and the transverse wave vectors can not adapt inside the crystal. The condition that has to be satisfied in the transversal direction can be written $|\Delta k_\perp|d \leq 1.18$, where d is the diameter of the beams [13] . If one assume small angles, the condition can be written

$$|k_p\theta_p - k_s\theta_s - k_i\theta_i|d < 1.18, \tag{2.31}$$

If we assume that the signal and idler have the same direction, $\theta_s = \theta_i$, which corresponds to the phase matching angle, the acceptance angle for the pump in the OPA can be estimated directly from Eq. 2.31. For the experimental setup used in this project, the pump acceptance angle is $\theta_p = 0.0007°$. This means that the angle between the pump and the signal and seed waves must be less than 0.0007° for the OPA to operate effectively. This estimation assumes however that the beams do not have any divergence. In real beams, the acceptance angles for efficient phase matching are much more complex because each of the waves consists of several angle components.

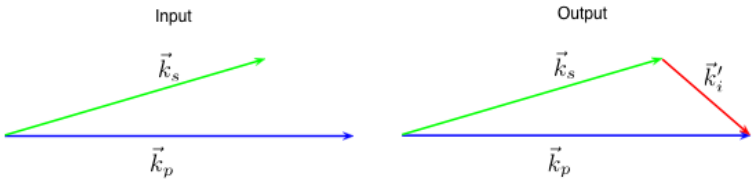

(a)

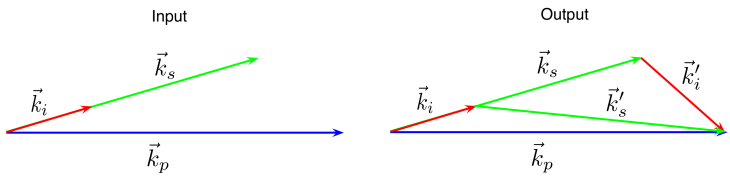

(b)

Figure 2.6: Two examples of how the directions of the output beams depend on the direction of the input beams. (a): Two beams with wave vectors $\mathbf{k}_p$ and $\mathbf{k}_s$ are used as input and generates a new output wave with wave vector $\mathbf{k}_i'$. (b): An additional beam with wave vector $\mathbf{k}_i$ is used as input which result in an additional output wave with wave vector $\mathbf{k}_s'$.

Fig. 2.6 shows a simplified effect if the direction of the input beams have different directions with $\Delta\mathbf{k} = 0$. In Fig. 2.6a, only signal and pump are incident on the crystal, and in Fig. 2.6b, all three beams are incident and signal and idler have the same direction. It can be seen that if both signal and idler are used as input beams and have different direction than the pump, the generated signal and idler will have different directions at the output, which is an undesired effect.

2.4 Optical Parametric Oscillator (OPO)

The gain of an OPA is modest even for high pump intensities. The net gain can be increased by providing positive feedback of the signal and/or idler beam. As mentioned in section 2.2, this can be done with an OPO, where a nonlinear crystal is placed inside a resonator. Initially, only the pump is incident on the crystal and the signal and idler grow from quantum noise (parametric fluorescence). When the pump power is above a certain threshold value, oscillation occurs and the signal and idler waves grow significantly. In the crystal, the pump, signal and idler waves overlap. The OPO is called singly resonant (SRO) when the resonator is resonant at either the signal or the idler wavelength, and doubly resonant (DRO) when both waves resonate. At steady-state operation, the gain of the oscillating wave(s) equals the loss. The loss includes

the loss due to out-coupling by one of the resonator mirrors, which provides the desired output. The output of the OPO is coherent radiation like that of a laser. The output frequencies of the OPO are determined by conservation of energy and momentum (Eq. 2.20). Tuning is thus achieved by controlling the refractive index using e.g. angle tuning.

The OPO resonator can be realized as a linear resonator consisting of two mirrors, or as a ring resonator with three or more mirrors. Fig. 2.7 illustrates three different resonator types. A ring resonator is more complex and more difficult to align, but have advantages such as prevention of strong pump feedback into the pump laser, and because the two beam passes in the crystal do not overlap, the fluence will be reduced. It is also easier to suppress non-resonant beams in the ring resonator because they can be coupled out at multiple mirrors. The lens effect induced by the thermal load is also effectively reduced.

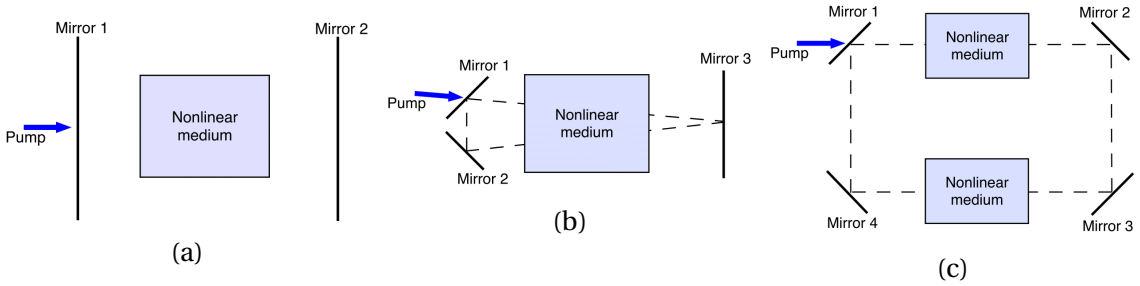

Figure 2.7: Three different realizations of the OPO resonator. (a): Linear resonator. (b): 3-mirror ring (V-shaped) resonator. (c): 4-mirror ring resonator with two nonlinear mediums.

2.4.1 OPO characteristics

The important characteristics of OPOs to be described include oscillation threshold, conversion efficiency, stability, bandwidth, tuning range, build-up time and beam quality. In this work, the most interesting parameters are those related to conversion efficiency and beam quality.

The conversion efficiency is simply defined as

$$\eta = \frac{E_s + E_i}{E_p}, \tag{2.32}$$

where E_p is the input pump energy and E_s and E_i are the output signal and idler energies.

For pulsed OPOs there will be a finite build-up time required to amplify the quantum noise to a steady-state signal power. This is because a certain amount of round-trips in resonator is required to make the signal power in the order of the pump power, and pump depletion will become evident. The build-up time is therefore related to the round-trip gain and the round-trip time of the OPO resonator. The pump energy that is sent through the resonator before the signal has grown strong enough to deplete the pump is wasted, hence a short build-up time is important for efficient operation. As higher the pump power is above threshold, the higher the initial gain in the OPO is, and the build-up time becomes shorter. However, too high pump power can result in back-conversion, which reduces the conversion efficiency.

The beam quality of a laser beam can be defined in different ways, but is normally understood as a measure of how a laser beam will diverge in the far-field or focus in the near-field [14]. Beam quality can be a critical parameter in the practical performance of a laser in a wide range of applications. The M^2 factor, also called beam propagation factor, is a common measure of a lasers beam quality. M^2 is defined as the ratio of the beam parameter product of an actual beam to that of an ideal Gaussian beam at the same wavelength. The best possible beam quality is achieved for a diffraction-limited Gaussian beam, having $M^2 = 1$. Smaller values are physically not possible. M^2 can be defined as

$$M^2 = \frac{\Theta \pi w_0}{\lambda}, \tag{2.33}$$

where w_0 is the beam radius in the near field and Θ is the far field beam divergence. From this formula it can be understood that if the beam should be used in a long-distance application where the beam size in the far field not should be too big, M^2 sets a limit for w_0. If M^2 is big, the value of w_0 would also have to be big, which often is unpractical. For the application purpose of this project, the design goal is $M^2 < 3$.

M^2 can be measured with different techniques. One common way is a fitting procedure, applied to the measured evolution of the beam radius along the propagation direction. Another tech-

nique is to measure the beam radius at the beam waist w_0 and the far field radius w. The far field radius can be measured in the focal plane of a positive lens, and the far field divergence is then given by

$$\Theta = \frac{w}{f}, \tag{2.34}$$

where f is the effective focal length of the lens.

A number of rules have to be observed, e.g. concerning the exact definition of the beam width. For arbitrary beam shapes, several different definitions such as FWe^{-2}M, FWHM and D4σ are common. The FWe^{-2}M width is equal to the distance between the two points on the marginal distribution that are $1/e^2 = 0.135$ times the maximum value. FWHM is the width measured between those points which are half the maximum amplitude. The D4σ method is based on the second moment of the intensity distribution. The D4σ width of a beam in the horizontal or vertical direction is 4 times the standard deviation, σ, of the horizontal or vertical marginal distribution, respectively. σ in the x-direction for a beam with beam profile $I(x,y)$ is expressed as

$$\sigma = \sqrt{\frac{\int_{-\infty}^{\infty}\int_{-\infty}^{\infty} I(x,y)(x-\bar{x})^2 dxdy}{\int_{-\infty}^{\infty}\int_{-\infty}^{\infty} I(x,y)dxdy}}, \tag{2.35}$$

where

$$\bar{x} = \frac{\int_{-\infty}^{\infty}\int_{-\infty}^{\infty} I(x,y)xdxdy}{\int_{-\infty}^{\infty}\int_{-\infty}^{\infty} I(x,y)dxdy} \tag{2.36}$$

is the centroid of the beam profile in the x-direction.

This method should be used particularly when trying to predict the evolution of the beam radius for not diffraction-limited beams. It has been shown that the usual rules for beam propagation with a certain M^2 factor then correctly describe this evolution, whereas errors occur when using beam radius defined in some other way [15].

2.4.2 Pump characteristics

The performance of OPOs and OPAs depends on the characteristics of beam used to pump the system. There are typically three different operation options for the pump laser; continuous wave (CW), Q-switched and mode-locked. Q-switched lasers typically produce nanosecond pulses and are most commonly used for pumping OPOs. If the pump has highly divergent components, these will not contribute to gain, due to the phase matching criterion. A pump with high beam quality is therefore important to achieve efficient conversion, especially in OPOs where acceptance intervals are small. The distribution of the pump power during the pulse and the pump energy have a major impact on the conversion efficiency of the OPO. The intensity distribution of the pump determines the spatial distribution of gain in the nonlinear crystal. A pump beam should have close to uniform intensity distribution in order to obtain efficient conversion.

The transverse profile of most laser beams will change during propagation. This means that even though the intensity distribution is close to uniform at the laser output, it might be deteriorated when it reaches the OPO or the OPA. This problem can however be reduced with a relay-imaging telescope containing two positive lenses with focal lengths f_1 and f_2, shown in Fig. 2.8. In both Fig. 2.8 and Fig. 2.9, $d_1 > 0$ to the left of lens 1, $d_2 > 0$ to the right of lens 1 and $d_3 > 0$ to the right of lens 2.

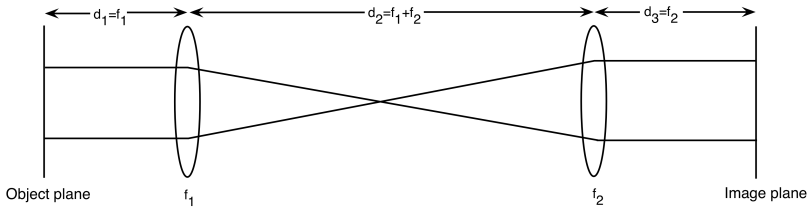

Figure 2.8: The relay-imaging telescope. The beam at the object plane is recreated in a scaled version at the image plane.

If the distance from the laser output to the lens with focal length f_1 is chosen to be $d_1 = f_1$, and the distance from the lens with focal length f_2 to the OPO/OPA is chosen to be $d_2 = f_2$, the beam in the OPO/OPA position is a scaled recreated version of the beam at the laser output The system

is characterized by the ABCD-matrix $\mathbf{M}_R$, which is shown in Eq. B.5 in Appendix D. The beam diameter is scaled by a factor f_2/f_1. In this way the beam diameter can be scaled to the desired size by choosing a telescope with appropriate focal lengths. A disadvantage of this telescope is the beam focus that is created between the two lenses. The fluence at the focus position can be extremely high, such that no optical devices should be placed near the beam focus. If the focal lengths are long, the system will also take up much place.

For high pump energies, typically used for pumping OPAs, the fluence at the beam focus can get so high that it leads to dielectric breakdown in air. In this case a Galilean imaging telescope, shown in Fig. 2.9, can be used to scale the beam diameter instead. Here, the first lens is concave instead of convex to avoid the focus.

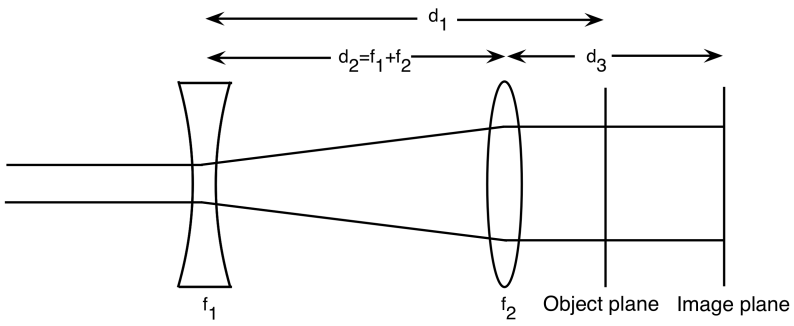

Figure 2.9: The Galilean telescope. In this telescope the distance d_1 has a negative value.

The ABCD-matrix $\mathbf{M}_G$ for the Galilean telescope is shown in Eq. B.6 in Appendix D. An example of the use of this telescope is taken from the experimental setup in this project: A lens with focal length $f_1 = -20$ cm is placed 133 cm behind the pump laser output and an OPA is placed in the image plane with distance $d_3 = 183$ cm behind a lens with focal length $f_2 = 30$ cm. The distance between the lenses is $d_2 = f_1 + f_2 = 10$ cm. From the ABCD-matrix it can then be found that the distance between lens 1 and the object plane is $d_1 = -88$ cm. This means that the beam in the OPA position is an image of the beam after it has propagated 221 cm from the laser output position. In other words, the transverse beam profile can look different in the OPA position than at the laser output with the use of the Galilean telescope.

2.4.3 Optical damage

Because laser light is usually delivered in beams with small transverse dimensions, it can easily cause laser-induced damage of optical components like mirrors, lenses, nonlinear crystals and photodetectors. As mentioned in the introduction, the damage threshold of a component or material can be specified with the allowable peak fluence. For a Gaussian beam, the peak fluence is the total optical energy divided by $\pi w^2/2$, where w is the Gaussian beam radius. From the time-dependent optical intensity, one can obtain the fluence by temporal integration over the full pulse duration.

Low damage threshold of nonlinear crystals limits the applicable optical energies in OPOs and OPAs. To avoid damage, it is important to determine the damage threshold of the crystal with the laser pulses used in the experiments and adjust the energy or beam diameter to keep the peak fluence below the threshold. Some laser beams exhibit "hot spots", i.e., regions with higher intensity, which may play role in damage phenomena. Hot spots can also occur when a laser beam propagates through an optical component with a damage. It is therefore important to detect the laser beam profile before it is used on an optical device and assure that there are no damages on the components the beam is propagating through.

2.5 Master Oscillator/Power Amplifier (MOPA)

Because of constraints imposed by crystal damage thresholds, scaling an OPO from low to high energy implies increasing the beam diameters to keep the fluence low. In a laser cavity, the Fresnel number is defined as $N_F = d^2/\lambda L$, where d is the beam diameter, λ the wavelength and L the length of the cavity. The result of an increased beam diameter is a high-Fresnel-number cavity that can support many transverse modes, often resulting in poor beam quality [16].

An approach to scale up the energy without compromising the beam quality is to use a master oscillator/power amplifier (MOPA) configuration consisting of a master OPO and one or more optical amplifiers to boost the output power. An illustration of a MOPA setup with one OPA is shown in Fig. 2.10. The basic idea behind such a configuration is to pump the OPO with a low to

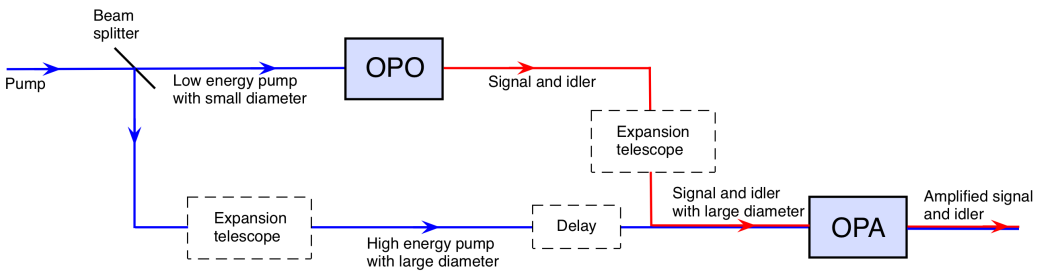

Figure 2.10: A two stage master oscillator/power amplifier (MOPA) configuration. The high energy pump beam is split into one beam with low energy directed towards the OPO and one beam with high energy directed towards the OPA. The beam used to pump the OPO have a small diameter to produce signal and idler beams with good beam quality. The signal and idler beams are then expanded and used as seed in the OPA which is pumped with the high energy pump beam with large diameter.

moderate energy beam, that optimized for providing output beams with good beam quality. A high-energy pumped OPA is then used to amplify the output beams from the OPO, resulting in output beams with good beam quality, also for beams with large diameter [17, 9]. Because there is a finite build-up time for the OPO output, the pump pulses used to pump the OPA should be delayed with a time corresponding to the build-up time such that the pump pulse and the seed pulse overlap in time in the OPA. This can be achieved by making the pump path length longer than the seed path length such that the time difference corresponds to the OPO build-up time.

2.6 ZGP Crystals

The ZGP crystals were manufactured by BAE systems, and were AR coated for the pump, signal and idler. ZGP is a positive uniaxial crystal and it has a large nonlinear coefficient, $d_{36} = 75 \pm 8$ pm/V [18], which makes it to one of the most efficient nonlinear crystals known. It is especially suitable for high average power applications because of its high damage threshold. The absorption coefficient of the crystals used in the experiments have been measured at the Norwegian Defense Research Establishment (FFI). In particular, at $\lambda = 2.05$ µm, $\lambda = 2.76$ µm and $\lambda = 8.00$ µm, the absorption coefficients are 10.7 m^{-1}, 4.7 m^{-1} and 3.7 m^{-1}, respectively. The ZGP transmission spectrum can be seen in Fig. 1.2 in the introduction chapter. The damage

threshold was investigated by reducing the pump diameter to 1 mm and visually inspect the crystal while the peak fluence was gradually increased in steps of 0.5 J/cm^2. The crystal was exposed for about 20 pulses in each step. Visual damage occurred for a peak fluence of 3 J/cm^2. During the experiments, the peak fluence was kept below 1.4 J/cm^2 to operate well below the estimated damage threshold.

Refractive index

The Sellmeier equation is used for the specification of a wavelength-dependent refractive index of a transparent optical material. The equation is usually on the form

$$n(\lambda) = \sqrt{1 + \sum_j \frac{A_j \lambda^2}{\lambda^2 - B_j}}, \tag{2.37}$$

where λ is the wavelength (in micrometers) of the incident light in vacuum and A_j and B_j are experimentally determined Sellmeier coefficients. The equation results from a physical model, which is applicable only to the wavelength region where the absorption is negligible. The literature contains a great variety of modified equations which are also often called Sellmeier equations. Extensions to Eq. 2.37 can enlarge the wavelength range of validity, or make it possible to include the temperature dependence of refractive indices. This can be important for calculating phase-matching configurations for nonlinear frequency conversion. Das et al. [19] derived a new set of Sellmeier equations based on refractive index measurements in a $ZnGeP_2$ crystal. The equation is

$$n(\lambda) = \sqrt{A + \frac{B\lambda^2}{\lambda^2 - C} + \frac{D\lambda^2}{\lambda^2 - E}}, \tag{2.38}$$

where the coefficients for ordinary and extraordinary polarization can be found in Table 2.2.

Table 2.2: Sellmeier coeffiecients for $ZnGeP_2$ crystal.

Polarization	A	B	C	D	E
Ordinary	5.67491	4.077926	0.159328	1.896005	900
Extraordinary	3.65014	6.310153	0.125099	1.731381	900

Table 2.3 shows the calculated values of n_o and n_e for the wavelengths of the beams involved in

the experiment.

Table 2.3: The ordinary and extraordinary refractive indices in ZGP for the relevant wavelengths.

λ [µm]	n_o	n_e
2.05	3.1472	3.1852
2.76	3.1343	3.1704
4.21	3.1228	3.1576
8.00	3.1013	3.1369

Effective nonlinearity

ZGP belongs to the crystal class $\bar{4}2m$. The expressions for the effective nonlinear coefficient for this class are

$$d_{eff} = d_{36} \sin 2\theta \cos 2\phi \qquad \text{(type I phase matching)} \tag{2.39}$$

$$d_{eff} = d_{36} \sin\theta \sin 2\phi \qquad \text{(type II phase matching)} \tag{2.40}$$

The angles θ and ϕ are defined in Fig. 2.4.

Phase matching calculations

In the OPO, the pump wavelength λ_p, signal wavelength λ_s and idler wavelength λ_i was 2.05 µm, 2.76 µm and 8 µm, respectively. The phase matching was of type II, such that the signal has a angle dependent extraordinary refractive index $n_s^e(\theta)$. By inserting the wavelengths and the constant refractive indices of the pump and idler into the phase-matching condition for a positive uniaxial crystal with phase-matching type II in Table 2.1, a value for $n_s^e(\theta)$ was found. The corresponding phase-matching angle θ_{pm} can then be found by inserting $n_s^e(\theta)$ into Eq. 2.21. The same procedure was used for the type II OPA1, where λ_p, λ_s and λ_i was the same as in the OPO, and for the type I OPA2, where λ_p, λ_s and λ_i was 2.76 µm, 4.21 µm and 8 µm, respectively. The azimuthal angle ϕ_{pm} of the phase matched direction was directly found from Eqs. 2.39 and 2.40; for type I, $\phi = 0°$ gives the maximum value of the nonlinear coefficient and $\phi = 45°$ gives maximum for type II. The calculated phase-matching angles are summarized in

Table 2.4. It should be emphasized that it is important that the refractive indices should have a precision of at least 4 decimals in the calculations.

Table 2.4: Phase matching calculations in ZGP. The idler wavelength is 8 µm in the calculatons and λ_s and λ_p shows which wave that is used as signal and pump.

λ_p [µm]	2.05	2.05	2.76	2.76
λ_s [µm]	2.76	2.76	4.21	4.21
Type	I	II	I	II
θ_{pm} [°]	50.6	63.3	47.5	65.9
θ_{cut} [°]	50	63	50	63
ϕ_{pm} [°]	0	45	0	45
ϕ_{cut} [°]	0	45	0	45

Chapter 3

Preliminary Simulations

Numerical simulations using realistic pump and crystal parameters were carried out to optimize the design of the MOPA system. In the OPO, variables such as pump diameter, crystal length, signal out-coupling and resonator configuration were investigated. Some parts of the OPO design, such as using a V-shaped resonator and type II phase matching, were based on previous results [20, 21]. Phase matching types were investigated in each stage of the OPA system with the goal of making an output idler beam at 8 μm with highest possible energy and good beam quality. The first OPA stage was simulated with both signal and idler as seeds, and signal only as seed.

3.1 Sisyfos

Sisyfos (Simulation system for optical science) is a program developed at FFI for simulation of optical parametric frequency conversion, lasers, and beam propagation in nonlinear or turbulent media. The main part of Sisyfos is a C++ library with classes corresponding to optical components such as beam sources, lenses, mirrors, and nonlinear crystals.

Sisyfos can include most of the physical effects that are relevant for frequency conversion and lasers such as diffraction, birefringence, dispersion, thermal effects, linear absorption, noise and multiple parametric processes in the same medium. The optical beams are represented in 3D arrays containing the complex amplitude as a function of transverse coordinates and

time. The objects that represent optical components have associated functions that transform a beam array in a way that corresponds to propagation through the component. By making a path that are calling such functions in a certain sequence, a simulation of the propagation through a whole device can be made.

Choosing suitable parameters for spatial resolution, matrix size, temporal resolution and time slice length is essential to get correct results when using Sisyfos. Because of symmetries in the OPO and OPA, the spatial mode used in the simulations was a half plane with $y \geq 0$ with (64,33) transverse points and a spatial resolution of 0.3 mm. In the temporal domain, Sisyfos works with time slices, where a time slice is treated as a unit when it propagates through the optical path. In OPO simulations with nanosecond pulses, where the pulses typically are longer than the round trip time, Sisyfos makes an approximation by treating time slices as isolated units. The time slices are then typically much smaller than the pulse length and Sisyfos assumes that the average power between time slices is the same as in the slices and scales up the energy correspondingly. The temporal parameters are *nt* (number of sample points per time slice), *dt* (time interval between sample points) and *tsi* (time interval between slices). Fig. 3.1 shows how the parameters are related. The spectral bandwidth is given by 1/dt and the spectral resolution will be 1/(nt × dt). In most of the simulations in this project, the temporal parameters were: nt=128, dt= 7×10^{-14} s and tsi=4.6046×10^{-10} s. When simulating the spectrum of the OPO, nt and dt were changed to 192 and 14×10^{-14} s to get a better spectral resolution.

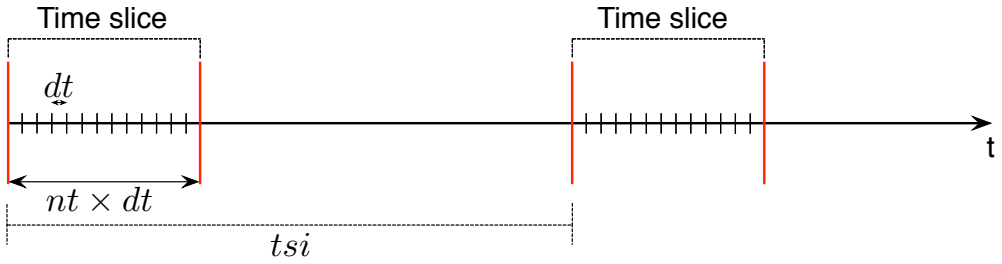

Figure 3.1: Time slices which are moving with the reference pulse. Each time slice consists of nt sample points with interval dt. Tsi is the time interval from the start of one slice to the start of the next.

By the laws of quantum optics, a loss necessarily introduces noise. Loss can be introduced in a Sisyfos model by absorption in a crystal, an aperture, or a partially transmitting mirror. In prin-

ciple, noise should be added at every lossy component, but to save time Sisyfos adds noise only when necessary. A realization of noise is computed by assigning a complex random Gaussian distributed amplitude to each mode and transforming back to real space-time. A consequence of the random noise is random fluctuations in the simulation results. For instance, the beam quality can vary with about 30 % from one simulation to another. The simulation results in this theses are therefore presented as the average from three different simulations.

3.2 OPO Simulations

Pump diameter

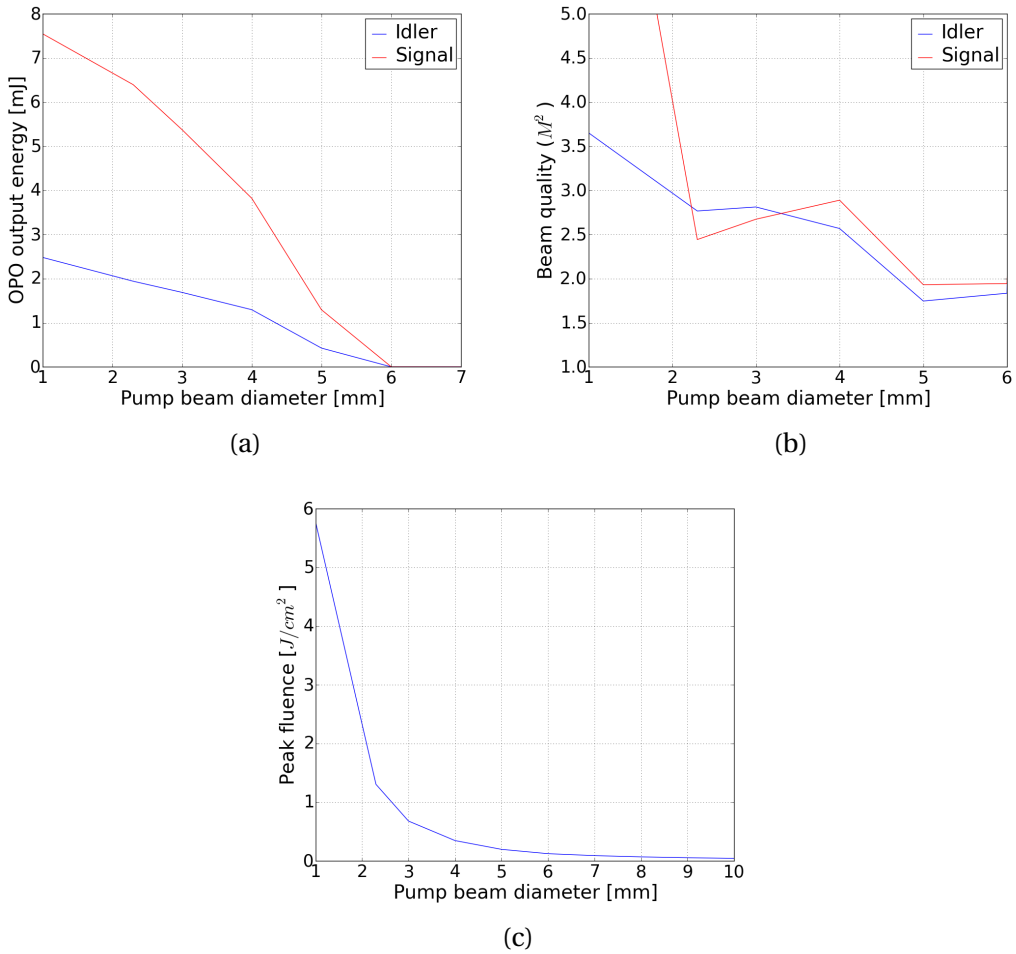

Figure 3.2: OPO output energy, (a), beam quality, (b), and peak fluence, (c), as functions of pump beam diameter. The pump energy was 22 mJ.

Fig 3.2 shows the simulated output energy, beam quality and peak fluence of the OPO with pump diameters ($FWe^{-2}M$) between 1 mm and 10 mm. OPO output energy refers to the total signal and idler energy. The pump energy was 22 mJ, the signal out-coupling 0.5, the crystal length 10 mm and the resonator was singly resonant for the signal. It can be seen that the output energy decreases when the beam diameter increases. However, the beam quality gets poor for diameters below 2 mm. To keep the peak fluence below 1.4 J/cm^2, the diameter has to be at least 2.2 mm. A beam diameter of 2.3 mm seems like a reasonable basis. This diameter results in a total output energy of 8.34 mJ with $M^2 = 2.4$ for signal and $M^2 = 2.7$ for idler.

Crystal length

Fig. 3.3 shows the results for crystal lengths in the range 4-16 mm. In the simulations, the pump diameter was 2.3 mm, the signal out-coupling 0.5, the pump energy 22 mJ and the resonator was singly resonant for signal. Fig. 3.3a indicates that a crystal length of 7 mm would be optimal in terms of conversion efficiency. Fig. 3.3b shows the relative delay between the OPO output and the pump pulses. Small delay means that the build-up time is short and the duration of the output pulses will be similar with the pump pulse. It can be seen that a crystal length of 9 mm would be optimal to get smallest delay. However, if the simulation result had been an average over many more simulations, the delay would most likely be a decreasing function of crystal length. Fig. 3.3c shows that M^2 is an increasing function of crystal length. To keep M^2 lower than 3, the crystal length should be smaller than 11 mm. The peak fluence was less than 1.4 Jcm^2 for all crystal lengths. According to these results, a crystal length of 7 mm or 8 mm would probably be the most optimal. However, a 10 mm crystal was already implemented in the OPO when these simulations were performed. A 10 mm crystal would also give a shorter build-up time than a shorter crystal, resulting in a more similar pulse duration of the pump, signal and idler beams.

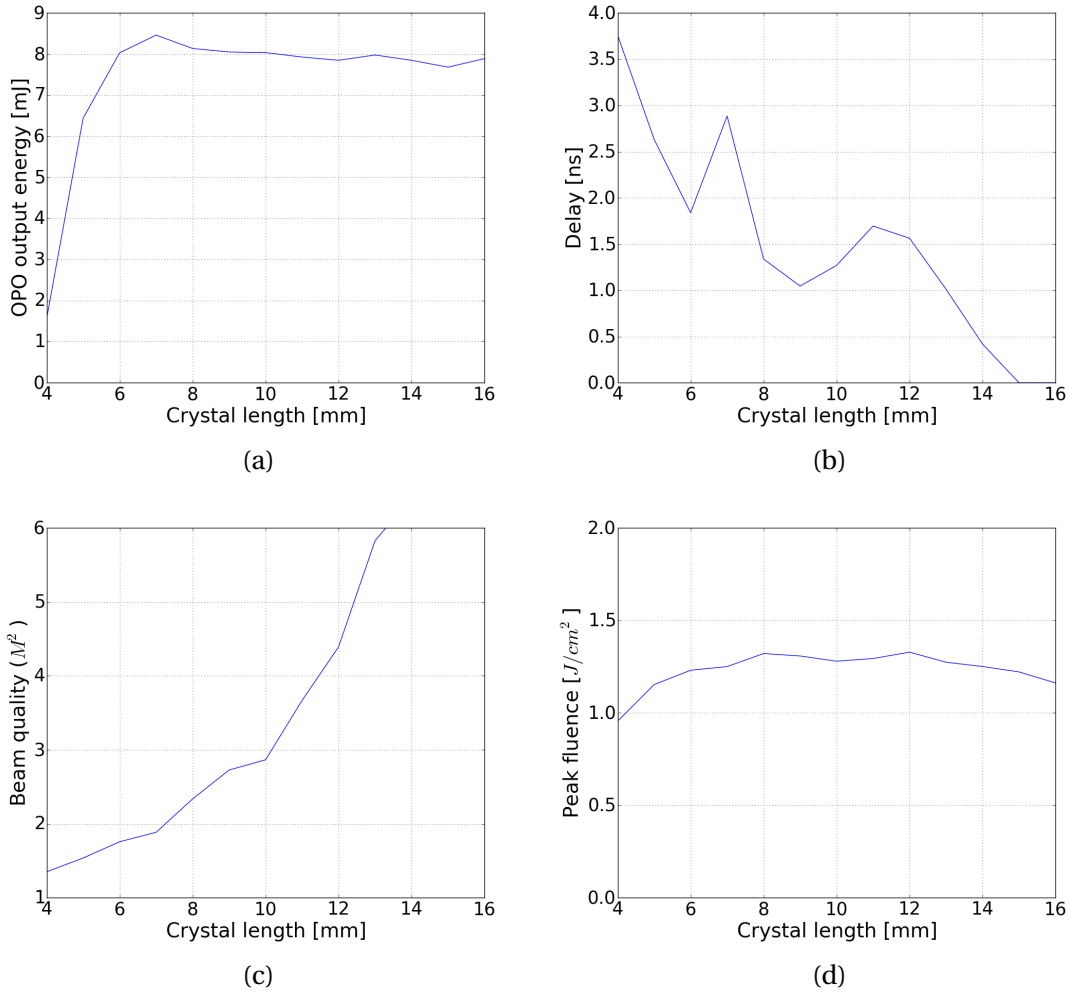

Figure 3.3: OPO output energy, (a), relative delay between signal and pump, (b), beam quality, (c), and peak fluence, (d), as functions of crystal length. The pump energy was 22 mJ. The fluctuations that especially can be seen in (b) is caused by the random quantum noise in the simulation.

Signal out-coupling

In the previous simulations, the signal out-coupling was 0.5. Fig. 3.4 shows simulations for a singly resonant OPO with a crystal length of 10 mm for signal out-coupling values between 0.2 and 0.7. It can be seen that low signal out-coupling gives high idler output energy, but at the cost of the beam quality. High out-coupling gives the best beam quality, but the idler energy gets lower. An out-coupling of 0.5 seems to be a good choice to give both good beam quality and sufficiently high idler energy. However, in this simulation, M^2 is higher than 3 for pump energies higher than 16 mJ for an out-coupling of 0.5. In Fig. 3.3c, M^2 is lower for a crystal with length

10 mm and an out-coupling of 0.5. This shows that there is some uncertainties in the simulation results, especially for the beam quality.

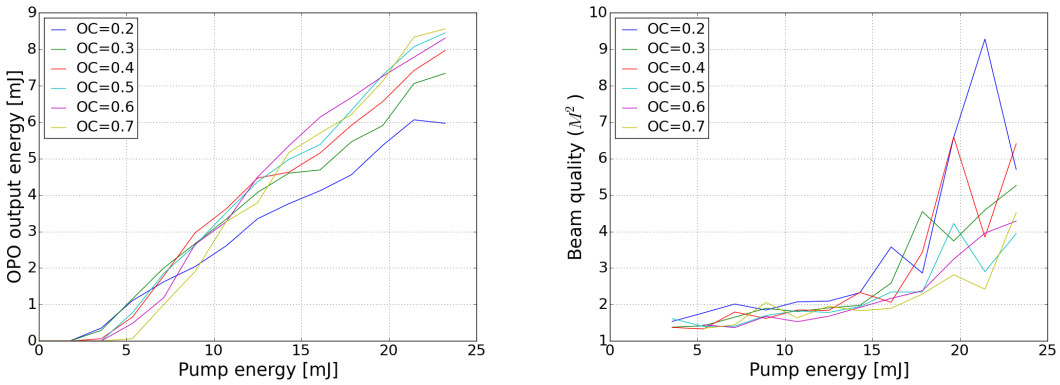

(a) (b)

Figure 3.4: Simulation results for a singly resonant OPO with a crystal length of 10 mm with different values for the signal out-coupling. (a) shows the idler output energy and (b) the idler beam quality as a function of pump energy.

Resonator type

As mentioned in section 2.4 in Chap. 2, an OPO resonator can be singly resonant or doubly resonant. A third alternative for a V-shaped resonator is a partly resonant configuration, where 100% of the idler beam is coupled out, but the two other mirrors are 100% reflective for idler. In this way, the idler that is generated in the return pass will not be wasted. Figs. 3.5a and 3.5b show the output energy and beam quality as a function of pump energy for the three different resonator alternatives. The crystal length was 10 mm and the pump diameter was 2.3 mm. It can be seen that the output energy is highest for the partly doubly resonant mode and lowest for the singly resonant mode. The threshold pump energy is lower for the doubly resonant mode. However, the beam quality increases drastically if the OPO is not singly resonant. For a pump energy at 22 mJ, M^2 is more than 3 times higher for the partly resonant mode than for the singly resonant mode. For the purpose of this project, a beam quality as a high as $M^2 = 10$ is too high, and it can be concluded that the best configuration is a singly resonant resonator.

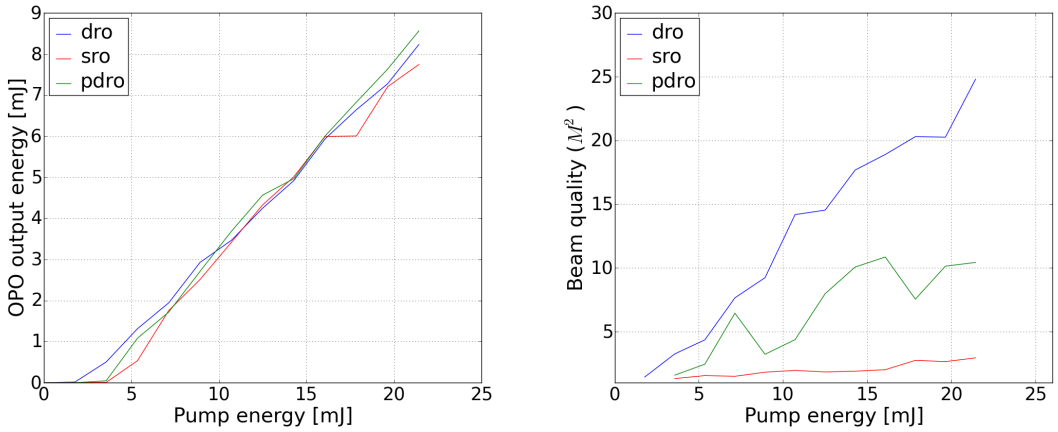

(a) (b)

Figure 3.5: OPO output energy, (a), and beam quality, (b), as functions of pump energy. The blue, red and green curves are the results for doubly resonant (dro), singly resonant (sro) and partly doubly resonant (pdro), respectively.

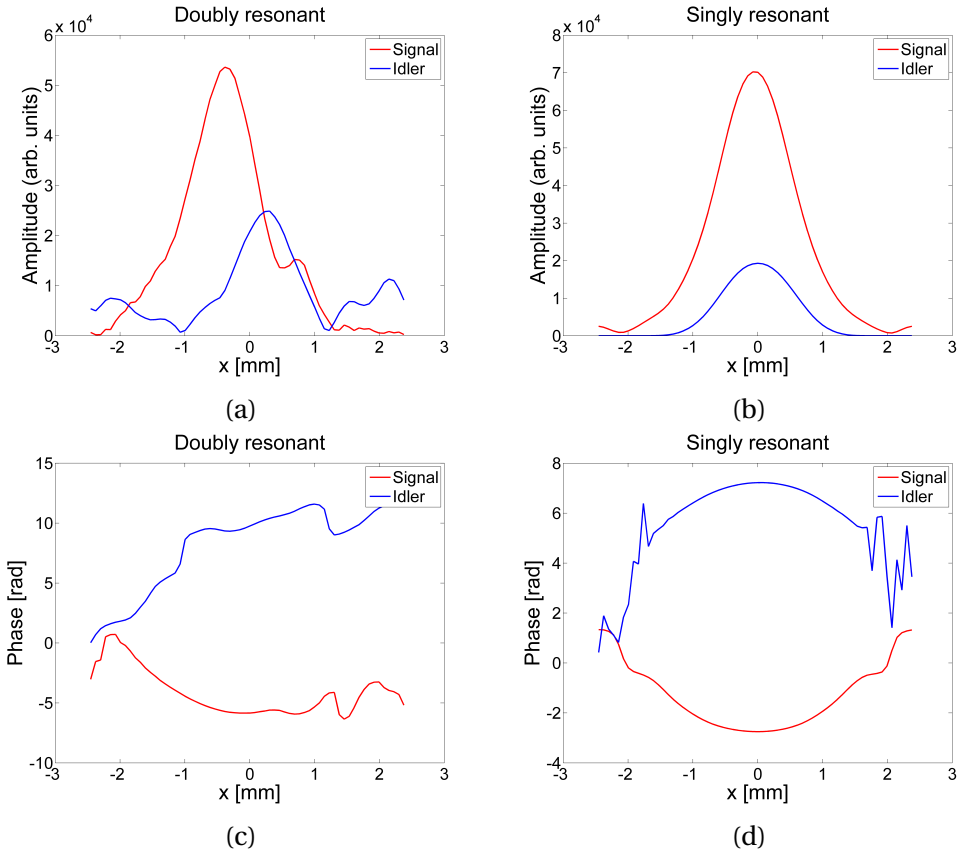

(a) (b)

(c) (d)

Figure 3.6: The amplitudes and phases of the signal and idler when the OPO resonator was doubly resonant, (a) and (c), and singly resonant, (b) and (d). The phase is only relevant where the corresponding amplitude not equals zero.

The reason why the beam quality is that much poorer when the resonator is not singly resonant, may be because it is more likely that back-conversion can occur when both signal and idler are present at the crystal entrance. If the intensity varies across the beam, back-conversion can take place in some transverse parts of the crystal and not others. The generated waves can thus get an arbitrary phase which leads to poor beam quality. The phase and amplitude of the signal and idler beams were investigated for the doubly and singly resonant OPO. Fig. 3.6 shows the amplitudes and phases in the x-direction at $y = 0$ and at a time approximately in the middle of the pulses. It can clearly be seen that the phase and amplitude for the doubly resonant OPO are more arbitrary than for the singly resonant OPO. However, it should be noticed that the idler amplitude in Fig. 3.6a does not go to zero near the edge of the matrix. This could be an indication that the transverse matrix used in the simulation was too small, and the results may therefore not reliable.

Summary

By summing up the OPO simulation results and taking the availability of crystals into account, a decision was made of using a ZGP crystal with length 10 mm, a pump diameter of 2.3 mm, a singly resonant resonator and a signal out-coupling of 0.5. According to simulations with a pump energy of 24 mJ, the OPO output should be an 1.9 mJ idler beam and a 6.5 mJ signal beam. M^2 was 2.4 for signal and 2.7 for idler. The peak fluence was estimated to be 1.4 J/cm^2. The simulated OPO output spectrum and power can be seen in Fig. 3.7. The idler has its peak at wavelength 7.976 µm and has a spectral width (FWHM) of 37 nm. The signal has its peak at wavelength 2.760 µm and has a spectral width (FWHM) of 3 nm.

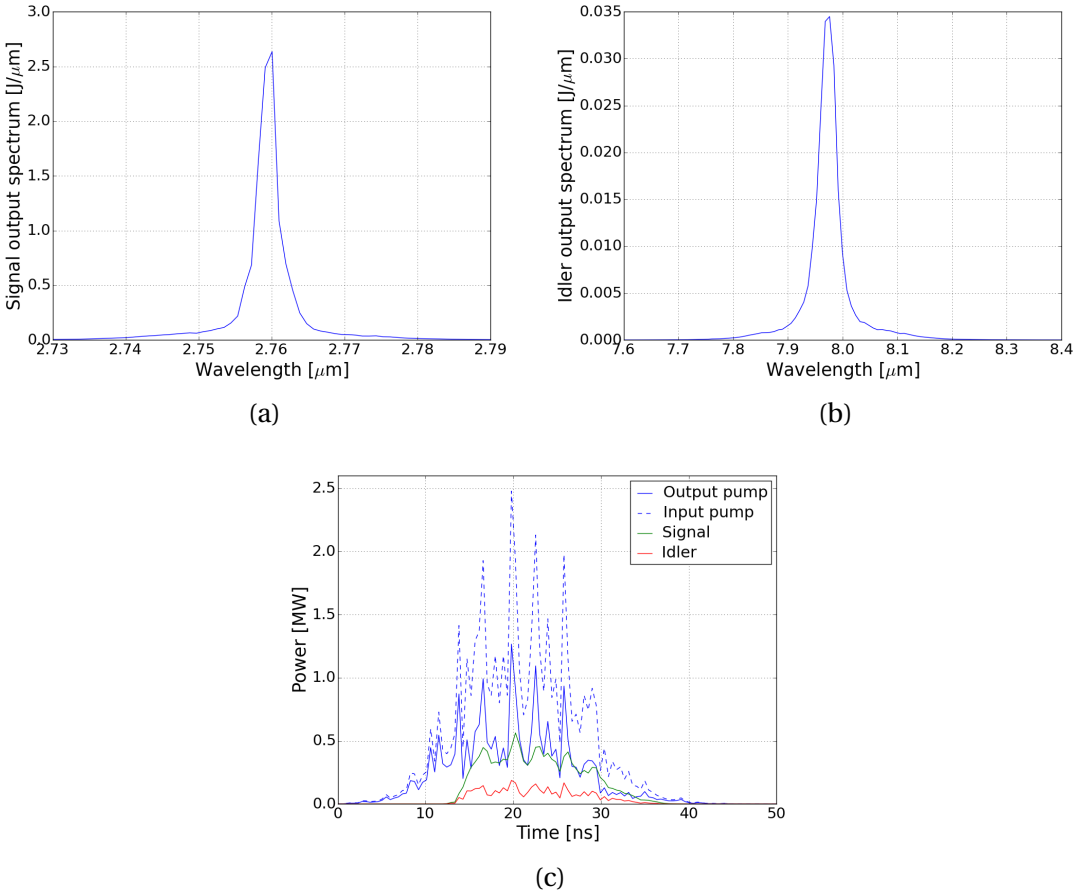

Figure 3.7: Signal spectrum, (a) and idler spectrum, (b), at the output of the OPO. (c) The input pump pulse and the output pump,signal and idler pulses.

3.3 OPA Simulations

OPA 1

Fig. 3.8 shows the simulated output energy and beam quality in the first stage OPA with type I phase matching for different crystal lengths, and Fig. 3.9 shows the corresponding results with type II phase matching. The dashed lines show the results when only signal was used as seed. The pump energy was 360 mJ, and the input signal and idler energy was 5.9 mJ and 1.69 mJ, respectively, when both idler and signal was used as seed. The input idler energy was set to zero when only signal was used as seed. The seed input was taken from the OPO simulations with some corrections because of losses in the path from the OPO to the OPA. The pump diameter was 8.9 mm and the diameter of the signal and idler was 9.9 mm.

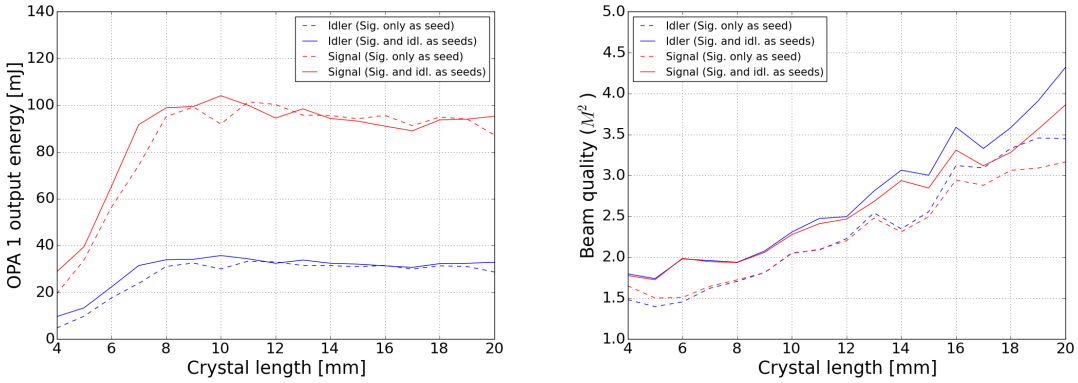

(a) (b)

Figure 3.8: Simulated OPA 1 output energy, (a), and beam quality, (b), for different crystal lengths in the first OPA stage with phase matching type I. Solid curves are used for signal and idler seed, and dashed curves are used for signal only seed. The pump energy was 360 mJ.

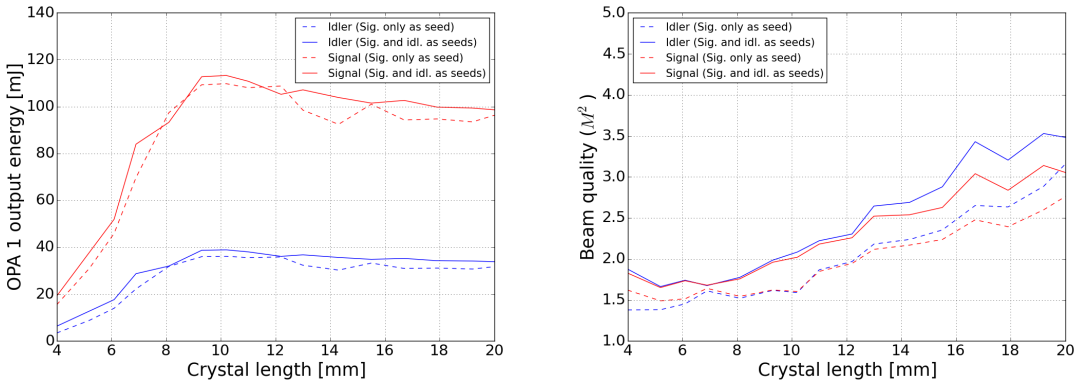

(a) (b)

Figure 3.9: Simulated idler output energy ,(a), and beam quality ,(b), for different crystal lengths in the first OPA stage with phase matching type II. Solid curves are used for signal and idler seed, and dashed curves are used for signal only seed. The pump energy was 360 mJ.

The simulations show that the difference in output energy when seeding with both signal and idler is very small compared with when seeding with signal only. The beam quality is however better when seeding with signal only. A type II OPA gives both the highest output energy and best beam quality compared to the type I OPA. The optimal crystal length for the type II OPA is 10 mm. This crystal length should give 38.8 mJ idler with $M^2 = 2.1$ when using both signal and idler as seeds, and 36 mJ idler with $M^2 = 1.6$ when only signal is used as seed. The corresponding

signal energy at the OPA output is 113 mJ when both signal and idler are used as seed, and 110 mJ when only signal is used as seed.

OPA 2

In the next OPA stage, the 2.76 µm signal beam will be used as pump to further amplify the 8 µm idler beam and generate a new 4.21 µm beam. If both signal and idler are used as seeds in the first OPA stage, the available pump energy in the second OPA stage will be 113 mJ and the available seed energy at 8 µm will be 38.8 mJ. Fig. 3.10 shows the output energy at 8 µm and the corresponding beam quality for different crystal lengths in the second stage OPA with type I and type II.

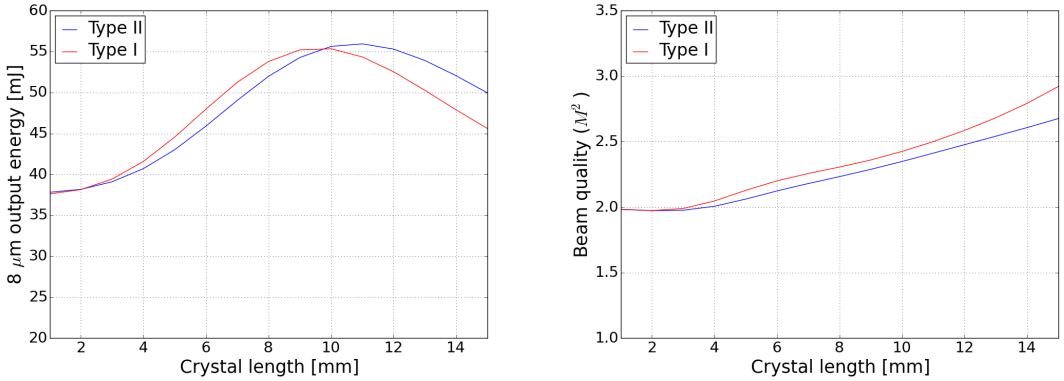

(a) (b)

Figure 3.10: Simulated idler output energy, (a), and beam quality, (b), for different crystal lengths in the second OPA stage with phase matching type I (red curve) and type II (blue curve).

The results show that when type I phase matching is used, the second OPA stage amplifies the output idler energy from 38.8 mJ to 55.3 mJ and gives $M^2 = 2.4$ when a 10 mm crystal is used. If type II phase matching is used, the idler energy is amplified to 55.9 mJ with $M^2 = 2.4$ when a 11 mm crystal is used. A second OPA stage with type II phase matching is however difficult to implement since the the pump (2.76 µm) and the idler (8µm) have different polarization after the first OPA stage.

Chapter 4

Experimental Procedure

4.1 Pump Laser

The laser used to pump the system was a Q-switched cryogenic Ho:YLF oscillator pumped by a Tm:fiber laser. The characterization of the laser beam is reported in Fonnum et al. [6], 2013. In this report pulses with energy up to 550 mJ was achieved by using 100 W of pump power for 35 ms. The pulses had a 14 ns FWHM duration at 1 Hz repetition rate and a central emission wavelength of 2051.3 nm, with a FWHM line width of 0.4 nm. The laser has a confocal unstable resonator with a graded-reflectance output coupler, resulting in a beam quality of M^2 = 1.5. However, during the experiments in this thesis, the maximum energy of the Ho:YLF laser using 100 W of pump power for 35 ms was 420 mJ. The diameter ($FWe^{-2}M$) of the beam was measured to be 6.3 mm and the pulse length (FWHM) was 25 ns. One of the reasons why the laser did not operate at the same energy, might be that the pump diameter was not correctly optimized.

4.2 Experimental Setup

A schematic of the experimental setup is given in Fig. 4.1. The Ho:YLF laser provides the 2.05 µm pump beam which was directed to a CaF_2 wedge. 30 mJ of the pump was picked off by the wedge and could be attenuated with the wave plate H1 and the polarizer P1. The polarizer only passed horizontally polarized light, so by rotating the wave plate, the pump energy to the OPO could easily be controlled. According to the simulation results, the pump energy to the OPO should

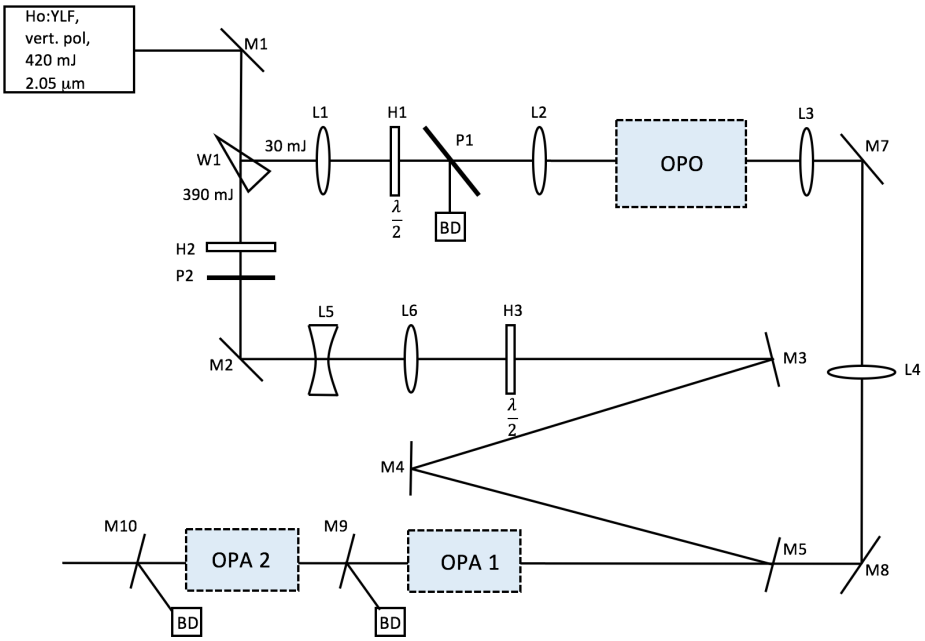

Figure 4.1: Schematic of the experimental setup. Mirrors are marked with M, lenses L, wedges W, wave plates, H and polarizers P. BD is short for 'beam dump'.

be maximum 24 mJ to keep the peak fluence below 1.4 J/cm^2. The lenses L1 and L2 had focal lengths 30 cm and 11 cm, respectively, and relay imaged the pump beam onto the OPO with a 2.3 mm FWe^{-2}M diameter. The lenses L3 and L4 had focal lengths 10 cm and 43 cm and form a relay imaging telescope that expanded the OPO output beam (signal and idler) to a FWe^{-2}M diameter of 9.9 mm. The mirrors M7 and M8 were Ag mirrors which directed the signal and idler beams towards OPA 1 where the beams joined the pump path. Mirror M5 had high transmission for signal and idler.

The 390 mJ of the pump energy that was transmitted through the wedge and could be attenuated with the wave plate H2 and the polarizer P2, such that the pump energy sent towards the OPAs could be regulated. The beam was thereby expanded to a FWe^{-2}M diameter of 9.5 mm with a Galilean telescope made out of the lenses L5 and L6 with focal lengths -20 cm and 30 cm, respectively. The half wave plate H3 rotated the polarization of the pump beam to be horizontally oriented. The mirrors M3, M4 and M5 reflected the pump beam towards OPA1. The reason for the extra mirror M4 was to make it easy to adjust the path length of the pump, such that the path length difference between the pump and the signal/idler corresponded to the build up time of

the OPO. The simulation in Fig. 3.3b showed that the delay was 1.4 ns. Mirror M4 was thereby positioned such that the pump path length from the wedge to the OPAs was 42 cm longer than the OPO path length, which gave the pump beam a delay of 1.4 ns. It would be more optimal to use the measured delay instead of the simulated delay, but unfortunately the power measurements were too inaccurate to calculate the delay. When the beams had propagated through OPA 1, the pump beam at 2.05 µm was reflected into a beam dump by mirror M9. The amplified beams at 2.76 µm and 8 µm were transmitted through mirror M9 and used as input in OPA 2.

All the lenses used in the setup were CaF_2 lenses and the focal lengths are written as the design focal lengths. Both Casix lenses and Thorlabs lenses, which were designed for wavelengths at 1500 nm and 588 nm, respectively, were used. For the signal wave, the focal lengths deviated less than 1% from the design focal lengths, so the relay-imaging system with the lenses L_3 and L_4 was close to correct for the signal. However, for the idler, the focal lengths could deviate with up to 24%, which means that the lenses should be placed in different positions to relay-image the idler beam correctly. This is a problem that was difficult to correct for since both idler and signal propagated through the same lenses. Since the idler and signal had wavelengths relatively far away from each other, it was important that the beams propagated exactly through the center of the lenses, or else they were spread into different directions.

A detailed list over all the components used in the experiments can be found in Appendix A.

4.2.1 Ring OPO

The OPO is illustrated in Fig. 4.2. It had a V-shaped 3-mirror ring resonator allowing for double-pass pumping in the same crystal, without overlapping forward and backward beams. Mirror M_1 and the out-coupler M_{out} were zinc selenide mirrors. M_1 was designed for having high transmittance (> 95 %) at 2.05 µm, high reflectance (> 99.5 %) at 2.76 µm and high transmittance (> 95 %) at 8 µm. Mirror M_2 was initially supposed to be identical to M_1, but damage occurred. A mirror with higher damage threshold was therefore used instead. This mirror was design to have high transmittance at 2.096 µm, high reflectance at 2.8-3.3 µm and high transmittance at 8-8.4 µm. The out-coupler, M_{out} was designed to have high reflectance (> 95 %) at 2.05 µm, 50%

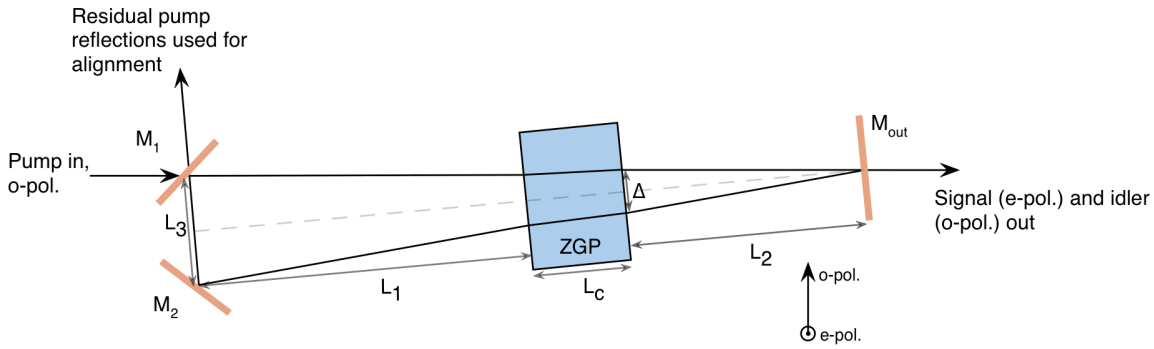

Figure 4.2: V-shaped ring resonator with two passes through the same crystal and angle tuning about an axis perpendicular to the plane of the ring.

reflectance at 2.76 µm and high transmittance (> 95 %) at 8 µm. This configuration makes the OPO single resonant.

The transmittance for mirror M_1 and M_{out} were measured with a FTIR spectrometer. Mirror M_2 was unfortunately to small to be measured. The measured transmission spectrums can be seen in Figs. C.1 and C.2 in Appendix C. In the measurements, M_1 transmitted 73 % of p-polarized light at 2.05 µm with 45° angle of incident, and had a reflectance of 96 % for s-polarized light at 2.76 µm and a transmittance of 72 % for p-polarized light at 8 µm. However, since the measured values had large deviations from the design-values, it was suspected that the FTIR measurements for this mirror were wrong. The transmittance of mirror M_1 at 2.05 µm was therefore measured directly with a energy meter, and was then found to be 95%. The out-coupler was measured to reflected 54 % at 2.76 µm and had high reflectance (99.9 %) at 2.05 µm and high transmittance (100%) at 8 µm.

Mirror M_1 and M_2 were placed close together in order to make the arm L_3 short. This makes the angle between the two other arms in the ring small enough to allow both of them to pass through the same crystal. The separation distance Δ should be at least comparable to the beam diameter ($FWe^{-2}M$) and was chosen to be about 3.6 mm. This is important in terms of the peak fluence. The round-trip distance in the resonator was 130 mm.

Simulations showed that the ideal crystal length was between 8 and 10 mm. Because of the availability of crystals, a crystal with length 10 mm and aperture 12 mm x 14 mm was used. The crystal was cut 63° for type II phase matching and the tuning axis was perpendicular to the plane in Fig. 4.2. The p-polarized pump and idler beams would then experience ordinary polarization inside the crystal, and the s-polarized signal would experience extraordinary polarization.

Mirror M_1 in Fig. 4.2 was fixed while the other two were adjustable. After establishing the desired angle on the output coupler, the input pump beam reflection from M_1 and the pump reflection from M_2 were observed with a pyro-electrical camera, and were adjusted to overlap in the near field and far field. After this overlap was established, the camera was placed after the out-coupling mirror to fine tune the resonator, such that signal and idler also overlap in the near and far field. Unfortunately, the pump laser was sensitive to humidity and the pump beam could slightly change direction from day to day. This made it necessary to fine tune the OPO every time it was used.

4.2.2 OPAs

Fig. 4.3 shows the schematic of the OPA system including OPA 1 and OPA 2. The simulations in Fig. 3.8 and Fig. 3.9 showed that OPA 1 should be of phase matching type II and the optimal crystal length was 10 mm when pumping with an energy of 360 mJ. The system was tested with crystals of both 10 mm and 12 mm, both cut for type II phase matching.

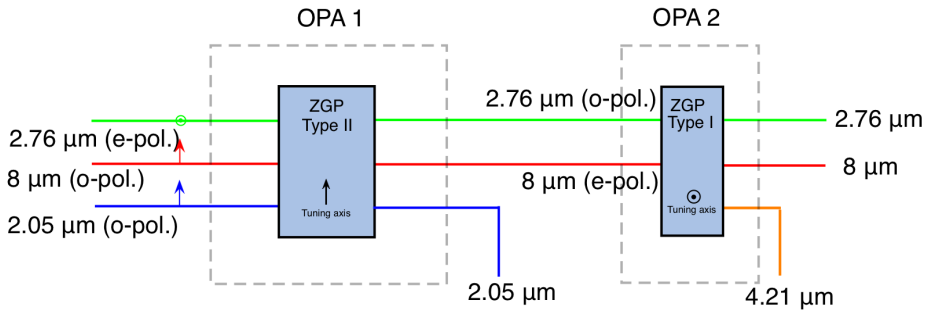

Figure 4.3: The OPA system including OPA 1 and OPA 2. The green, red and blue line represent the 2.76 µm, 8 µm and 2.05 µm beams, respectively. The arrows on the beams shows the polarization direction of each beam and the arrows inside the crystal shows the tuning axes.

For the 12 mm crystal, a combination of crystals of 8 mm and 4 mm was used because none of the available crystal had a length of 12 mm. The tuning axis in OPA 1 was parallel with the paper plane in Fig. 4.3. This gives the signal (2.76 µm) extraordinary polarization and idler (8 µm) and pump (2.05 µm) ordinary polarization. After the beams had passed OPA 1, a mirror with high reflectance for 2.05 µm and high transmission for 2.76 µm and 8 µm was used to dump the 2.05 µm pump beam. The signal beam at 2.76 µm then worked as a pump to give further amplification to the 8 µm beam in the type I OPA 2. The new 4.21 µm beam generated in OPA 2 was dumped by using a new mirror of the same type as used after OPA 1, which also had high reflectance for 4.21 µm. The measured transmission at the different wavelengths in the mirror used to dump the 2.05 µm and 4.21 µm beams can be seen in Fig. C.3 in Appendix C. The losses in the mirrors was accounted for when measuring the output energy at 8 µm and 2.76 µm.

The experimental setup was tested with both signal and idler as seed and just signal as seed in the OPA 1. For the latter, the idler beam was removed by placing a short wavelength pass filter in the beam propagation path before the OPA. The loss in the filter was about 10 %, such that the signal input energy was less when just signal was used as seed. In-out curves and idler beam quality were measured after both OPA 1 and OPA 2.

4.3 Measurements

4.3.1 Spectrum

The spectrum of the OPO output was measured with a diffraction grating spectrometer with focal length $f = 24$ cm. The beams were first focused by a lens with a focal length of 10 cm onto the entrance slit to get higher intensity. The entrance slit size d and the groove density of the grating n were adjustable. The parameters used when measuring the signal and idler can be seen in Table 4.1. A detector and a digital oscilloscope were used to record the spectrum. The resolution of the spectrometer is given by $R = \lambda/\Delta\lambda = nW$, where $\Delta\lambda$ is the smallest resolvable wavelength difference and W is the width of the illuminated grid. Under the assumption of small angles, the resolution can be written $R \simeq nf\lambda/d$.

Table 4.1: The parameters used in the spectrometer when measuring the spectrum of the signal and idler output from the OPO.

	d [µm]	n [mm^{-1}]	R	$\Delta\lambda$ [nm]
Signal	50	300	3974	0.7
Idler	30	75	4800	1.7

4.3.2 Pulse power

The pulse power of the pump pulse was measured from the pump beam that was transmitted through mirror M_2 in Fig. 4.2. The beam was first directed onto a rock and then using a detector to detect the reflected beams from the rock. The reason for why the beams could not be detected directly was the low damage threshold of the detector. Both the depleted and undepleted pump pulses were measured. To measure the undepleted pump pulse, a thin card was placed between mirror M_1 and M_2 in the OPO to stop the conversion process. The signal pulse was measured in the same way from the output beam of the OPO. The detector was connected to an oscilloscope which could plot the power as a function of time. The measured energies of each beam was later used to calibrate the power.

4.3.3 In-out energy curves

In-out energy curves were measured for the OPO, the OPA 1 and the OPA 2 with a pyroelectric energy meter. The input energies were measured by placing the energy sensor in a position right in front of the OPO/OPA and writing down the measured energy while rotating the wave plate from minimum to maximum energy in steps of 5°. The same procedure was thereafter performed with the energy sensor placed behind the OPO/OPA. It should be noticed that the input pump energy for the OPO was defined as the energy in front of the in-coupling mirror, not in front of the crystal. To measure the idler and signal energy separately, a polarizer was used to only pass the wanted wave. The loss in the polarizer was simply estimated by measuring the energy of a beam with a single polarization state before and after the polarizer. The loss was found to be 3% and was accounted for when measuring the energy of the idler and signal.

4.3.4 Beam quality

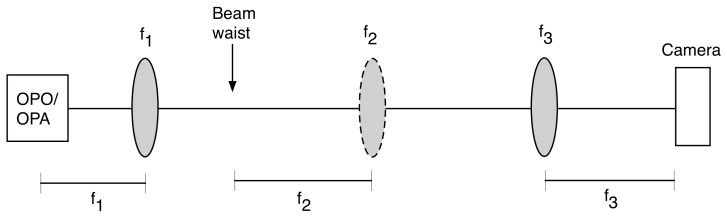

Figure 4.4: Schematics of the setup for measuring beam quality. The lens with focal length f_1 is used to make a new waist. An image of this waist with magnification f_3/f_2 can be taken when lens 2 is placed a distance f_2 from the waist and the camera is placed a distance f_3 behind lens 3. The far field can be imaged by removing lens 2.

As explained in Sec. 2.4.1, both the radius of the beam in near field and in the far field must be determined to measure the beam quality. The method used to find M^2 is illustrated in Fig. 4.4. Lens 1 with focal length f_1 was first placed after the OPO/OPA to make a new beam waist. Lens 2 and lens 3 constitute an imaging system if lens 2 is placed a focal length f_2 behind the waist and the camera is placed a focal length f_3 behind lens 3. Lens 2 was moved in steps of ~ 0.5 cm to find the position of the beam waist, i.e. the near field. By removing lens 2, the camera could detect the far field. The focal lengths of the lenses was chosen such that the beam has an appropriate size compared to the camera detector and the pixel size. The focal lengths used for the different beam quality measurements are listed in Table 4.2.

Table 4.2: The focal lengths for $\lambda = 8$ µm used in the idler beam quality measurements. The focal lengths are corrected values of the design focal lengths by taking dispersion in the lens material into account.

	f_1 [cm]	f_2 [cm]	f_3 [cm]
OPO	12.1	12.1	36.3
OPA 1, 10 mm	121	26	31
OPA 1, 12 mm	121	24.4	31
OPA 2	121	24.4	31

The D4σ radius of the beam in the near -and far field was found by analyzing the images in Matlab. When the D4σ was appropriately calculated, Eqs. 2.33 and 2.34 were used to calculate M^2. M^2 can be difficult to measure accurately, and factors such as background noise can create

large errors. It is therefore important to subtract the baseline of the beam profile, such that the average noise equals zero. However, experience shows that by changing for instance the aperture of the image or the saturation on the camera, M^2 measurements can deviate by a factor ~ 0.05. It is therefore meaningless to express M^2 with an accuracy better than 1 decimal.

Chapter 5

Results and Discussion

5.1 OPO

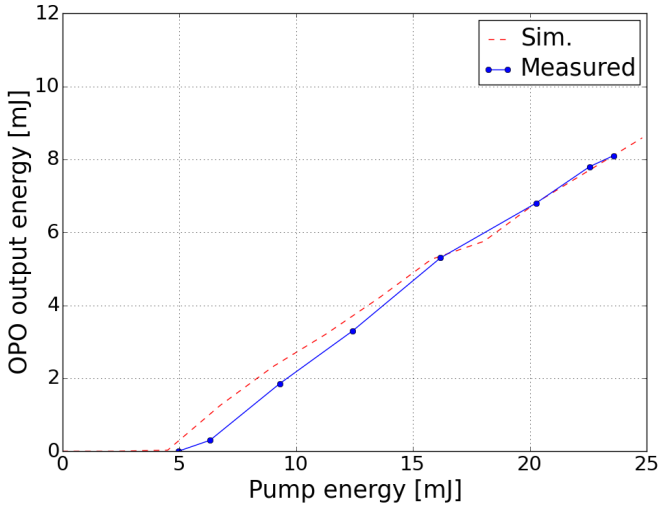

Figure 5.1: The measured output energy (signal + idler) from the OPO (blue curve). The red curve shows the simulated output energy.

Fig. 5.1 shows the measured output energy from the OPO, including both signal and idler. The dashed red curve shows the simulated result, where the pump energy was corrected for 95% loss in the in-coupler mirror. In the experimental measurement, the pump energy threshold was 5 mJ, which is in good agreement with the simulation. When pumping with 24 mJ, the OPO output energy was 8.1 mJ (6.3 mJ signal and 1.8 mJ idler). This corresponds to a conversion efficiency of $\eta = 0.34$. The estimated peak fluence inside the OPO at this energy was 1.35 J/cm^2.

One of the reasons why the output energy was slightly lower than in the simulations might be that the OPO was not perfectly aligned. Since the OPO could get out of alignment from day to day, the output energy could also vary and the conversion efficiently was better some days than others.

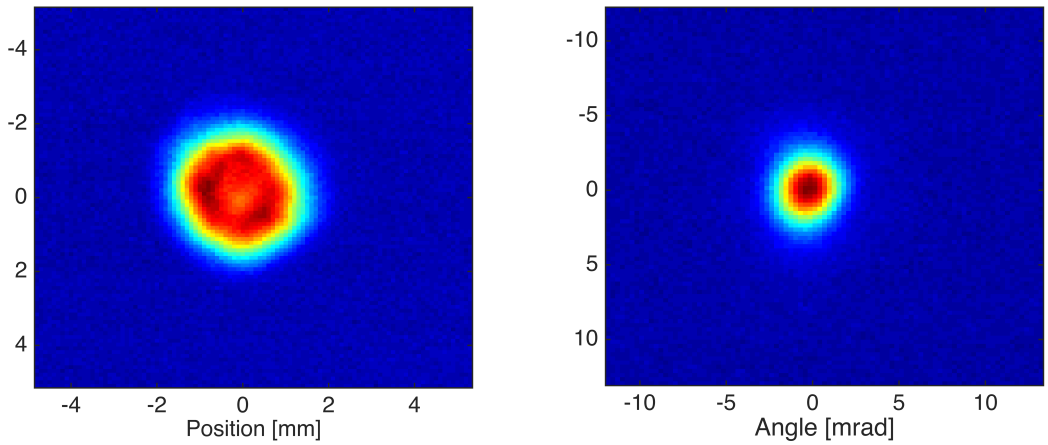

(a) (b)

Figure 5.2: Measured near field (a) and far field (b) of the idler output from the OPO when pumping with 24 mJ.

Fig. 5.2 shows the fluence distribution of the output idler from the OPO in the near field, Fig. 5.2a, and in in the far field, Fig.5.2b, when pumping with 24 mJ. The beam quality was calculated by estimating the D4σ radius of the images as explained in Section 4.3.4. At maximum pump energy, the idler beam quality was measured to be $M^2 = 2.6$, which is in good agreement with the average beam quality in the simulation results. The beam quality of the signal was $M^2 = 2.1$. An overview of the performance parameters can be seen in Table 5.1.

Table 5.1: Measured performance parameters of the OPO.

Crystal length	10 mm
Pump energy	24 mJ
Peak fluence	1.35 J/cm^2
Signal output energy	6.3 mJ
Idler output energy	1.8 mJ
Efficiency	34%
Signal beam quality [M^2]	2.1
Idler beam Quality [M^2]	2.6

Since the ZGP crystal was cut at the phase matching angle $\theta = 63°$ for generating waves at

2.76 µm and 8 µm, the spectrum was measured without any tuning of the crystal. The measured specrum of the signal and idler can be seen in Fig. 5.3. The atmospheric transmittance spectrum (USA model, mean latitude, zero altitude, summer) for radiation that has propagated 2 meters is shown together with the signal spectrum. It can be seen that there are many absorption lines near the signal spectrum.

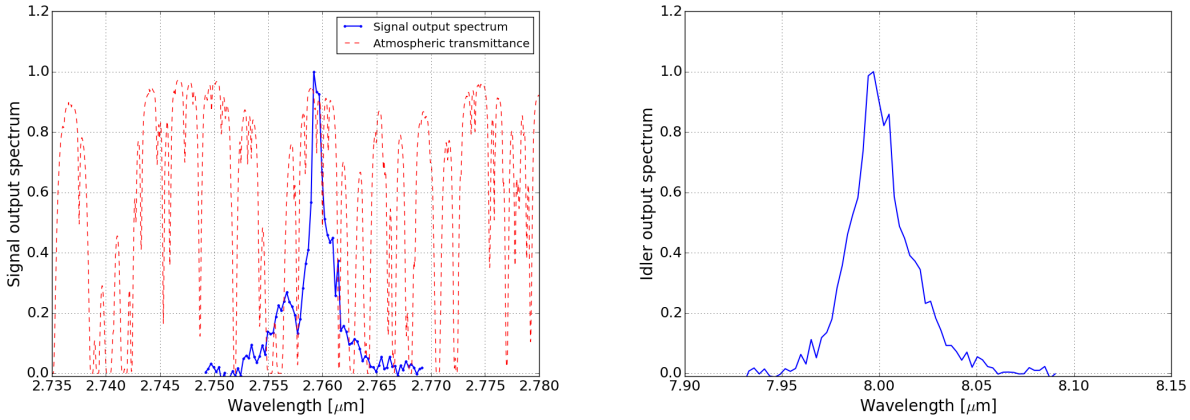

(a) (b)

Figure 5.3: Measured OPO output spectrum (normalized) of signal (a) and idler (b). The red rippled curved in (b) shows the atmospheric transmittance spectrum which has strong absorption lines in the signal spectrum.

The spectrometer was not calibrated before the measurements, so the signal spectrum was corrected by moving it 2.2 nm such that the local minimums of the signal curve fitted best with the atmospheric absorption lines. The signal peak wavelength was then found to be 2.759 µm with a FWHM spectral width of 2 nm. It looks like the spectrum is cut because of one of the absorption lines, so the spectral width might be narrower than it would have been without water vapor absorption. The position of the idler spectrum in Fig. 5.3b was corrected according to energy conservation, knowing that the pump peak wavelength was 2051.3 nm. The idler peak wavelength was then found to be 8.00 µm with a FWHM spectral width of 25 nm.

The measured power shapes of the pump and signal after the OPO can be seen in Fig. 5.4. The undepleted pump pulse with 25 ns duration is also shown. The power of the pulses was scaled such that the pulse energies corresponded with the measured energies of the beams. The signal had a pulse duration (FWHM) of 18 ns. The pulse that occurs after $t = 60$ ns is unphysical and

may be caused by the imperfect impulse response of the detector. The measurement shows that the depleted pump pulse has more power than the undepleted pump pulse when $t \simeq 12$ ns, which is not physically possible. This implies that the measurement is inaccurate. The difference between the depleted and undepleted pump pulse should in theory be zero when the signal pulse goes to zero, but in the measurement the difference is about 0.1 MW. The idler pulse was unfortunately not found by the detector, but it can be expected that the idler pulse will have the same duration as the signal pulse.

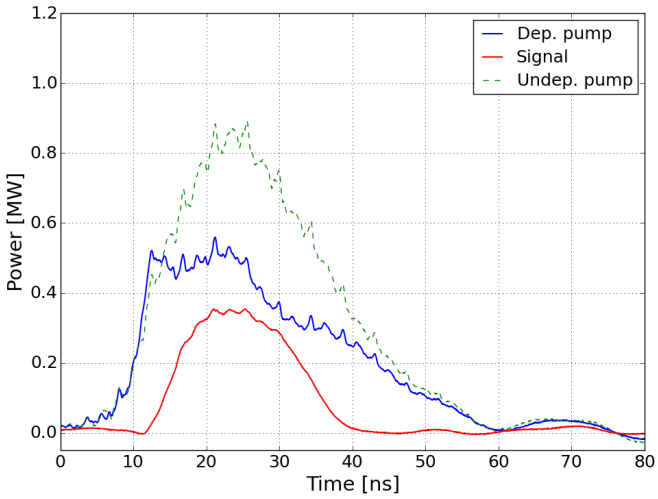

Figure 5.4: The measured pump pulses from the OPO. Green dashed curve: Undepleted pump. Blue curve: Depleted pump. Red curve: Signal.

5.2 OPA 1

The output energy of the OPO was directed along the pump path and used as input seed in the first OPA stage. Because of water absorption in the air, some of the signal energy was absorbed when traveling along the path from the OPO to the OPA. How much depended on the air humidity, which could vary from day to day. When the OPA measurements were performed, the signal energy was measured to be 4.3 mJ and the idler 1.7 mJ at the input position of OPA 1. This means that the signal loss was approximately 32 % and the idler loss was 5.6 %.

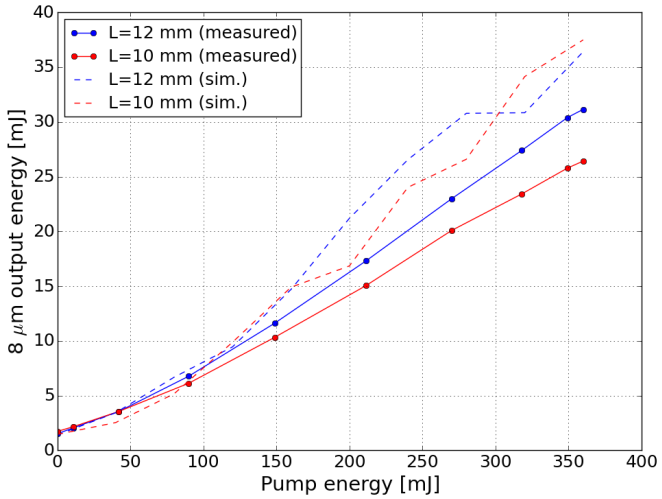

Figure 5.5: Measured output idler energy from OPA 1 with crystal length $L = 10$ mm (red curve) and $L = 12$ mm (blue curve). The dashed curves show the simulation results with the same seed energy as in the measurements. The pump energy was 360 mJ and both signal and idler were used as seeds.

The measured and simulated output idler energy for the 10 mm and 12 mm crystal when both signal and idler were used as seeds can be seen in Fig 5.5. It can be seen that the 12 mm crystal gave the best conversion efficiency. For the maximum pump energy of 360 mJ using the 12 mm crystal, 31.1 mJ at 8 µm was achieved with a beam quality $M^2 = 2.5$. The maximum output signal energy was 82.6 mJ. This corresponds to a conversion efficiency of 30 %. When the 10 mm crystal was used, the maximum output idler energy was 26.4 mJ with $M^2 = 2.9$. The output signal energy was 68.2 mJ. The corresponding conversion efficiency was in this case 26%. Measurements were also performed using only signal as seed. The input signal energy was then however reduced from 4.3 mJ to 3.8 mJ because of the loss in the short-wavelength-pass filter used to remove the idler beam. All the experimental results from OPA1 are listed in Table 5.2. The near field and far field fluence distributions of the idler after OPA 1 when seeding with both

Table 5.2: Measured performance parameters of OPA1. L denotes the crystal length.

	L [mm]	E_p [mJ]	E_i^{in} [mJ]	E_s^{in} [mJ]	E_i^{out} [mJ]	M^2
Signal and idler as seeds	10	360	1.7	4.3	26.4	2.9
	12	360	1.7	4.3	31.1	2.5
Signal only as seed	10	360	0	3.8	20.3	2.3
	12	360	0	3.8	26.0	2.0

signal and idler can be seen in Fig. 5.6.

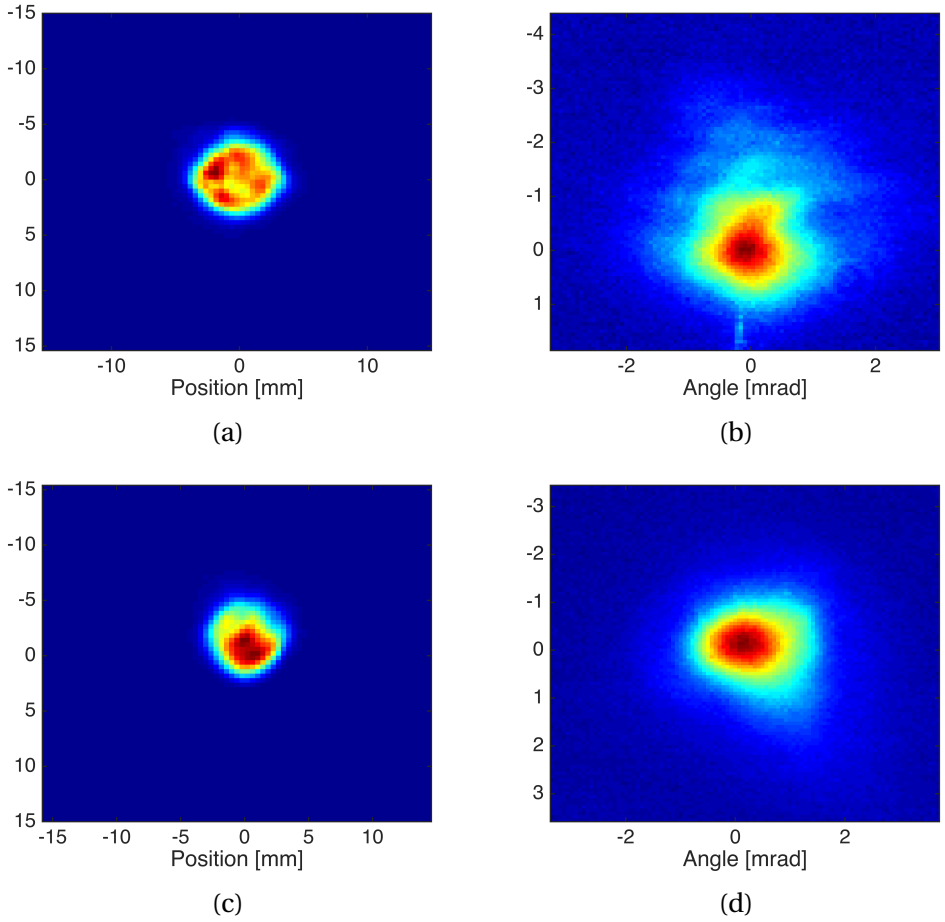

Figure 5.6: (a) and (b) shows the measured near field and far field of the 8 µm idler output from OPA 1 with a crystal length of 10 mm. (d) and (c) shows the corresponding near- and far fields for the 12 mm crystal. The pump energy was 360 mJ and both signal and idler were used as seed.

From Fig. 5.5, it can be seen that the conversion efficiency in the simulated results are better. The reason might be that the beam sizes of the real beams were different than in the simulations. If the real beams had a larger diameter than estimated, the output energy would be lower than expected.

For both the 10 mm and 12 mm crystals, the results show that the beam quality was better when signal only was used as seed. As explained in Section 2.3.4, when using three input beams, the idler output can consist of two separate beams, the amplified input idler and the generated

idler, if the input beams have different directions. This effect was observed on the camera. By adjusting the mirrors, it was possible to make the beams overlap. However, even though the idler beams overlap, it is possible that the beam quality will be affected. The output idler energy was also higher when seeding with both signal and idler, and according to simulations, M^2 will increase if the energy is increased. In the results in Table 5.2, the input signal energy was higher when both signal and idler were used as seeds, than when only signal was used as seed because of the filter. To further investigate if the conversion efficiency was higher when both signal and idler were used as seeds, a new measurement was performed where the signal seed energy was the same in both measurements.

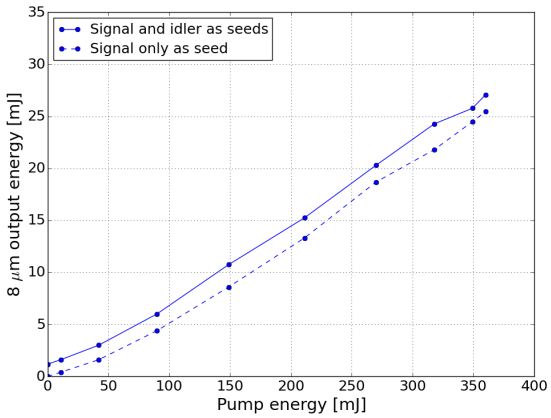

Figure 5.7: Idler output energy from the first OPA stage (OPA 1). Solid curve: Signal seed energy=3.8 mJ, idler seed energy=1.1 mJ. Dashed curve: Signal seed energy=3.8 mJ, idler seed energy=0 mJ.

The solid curve in Fig. 5.7 shows the measured output idler energy when seeding with 3.8 mJ signal and 1.1 mJ idler, while the dashed curve shows the measured output idler energy with only 3.8 mJ signal seed. From this result it can be seen that using idler as seed in addition to the signal seed, did not affect the conversion efficiency of OPA 1. The higher output idler energy simply corresponded to the input idler energy, but no more gain was achieved. Since the alignment was more difficult and the beam quality was poorer when operating with three input beams, the best configuration would probably be to seed with only signal or idler and use a filter or mirror with low absorption at the signal wave to remove the idler. Seeding with only one beam, would also resolve the dispersion problems that occurred when both signal and idler propagated through the same in the lenses.

An observation about the 4 mm crystal used in the compound 12 mm crystal was made when the pump beam had propagated through the crystal. Fig. 5.8 shows the fluence distribution of the beam before, (a), and after ,(b), the crystal was inserted in the beam path. It can clearly be seen that the beam was highly distorted after propagation through the crystal. There were no observable damages on the crystal coating, so the distortion was probably caused by defects inside the crystal. The effect might have affected both the beam quality of the generated beams and the conversion efficiency for 12 mm OPA 1.

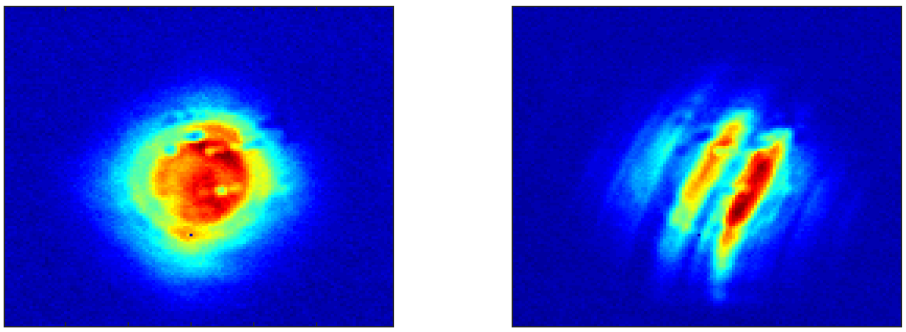

(a) (b)

Figure 5.8: The pump beam fluence distribution before, (a), and after, (b), the 4 mm crystal was inserted in the beam path. The defects in (a) was caused by damages on the camera filter.

Damage

When the 10 mm crystal was used, a damage in the crystal coating unfortunately occurred when pumping at maximum energy. An image of the damage can be seen in Fig. 5.9. After the damage occurred, the beam profile was investigated with the camera. It was then seen that the pump beam was strongly distorted and had several hot spots, which probably was responsible for the damage. It was found that the pump wave was distorted because of a laser induced damage on mirror M5 (see Fig. 4.1. This mirror was changed to a new similar mirror. No other ZGP crystals of type II and with a length of 10 mm was available, so all the results where the crystal length in OPA 1 is 10 mm, the damaged crystal was used. The damage was probably the reason why the far field fluence distribution in Fig. 5.6b shows a pattern that can look like interference ”ripples”.

The damage was also probably the reason why the beam quality was poorer when using the 10 mm crystal than the 12 mm crystal, even though the simulations implied the opposite.

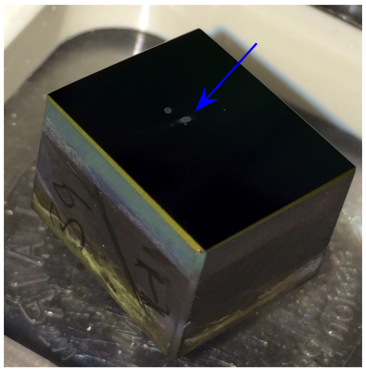

Figure 5.9: Optical damage on the coating of the 10 mm ZGP crystal caused by hot spots in the pump beam profile.

5.3 OPA 2

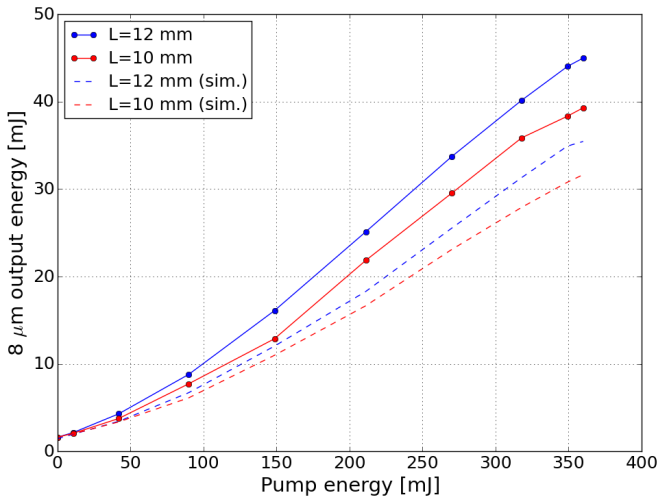

Figure 5.10: Measured output idler energy from OPA 2 with a crystal length of 5 mm. The crystal length in OPA 1 was 10 mm (red curve) and 12 mm (blue curve). The dashed curves show the simulation results. Both signal and idler was used as seeds in OPA 1.

Fig. 5.10 shows the measured (solid curves) and simulated (dashed curves) idler output energy from the second OPA stage (OPA 2) for the two cases where OPA 1 had crystal length 10 mm and 12 mm. Both signal and idler were used as seeds in OPA 1. The maximum measured energy at

8 µm was 45 mJ with M^2 = 3.1, which was achieved when the crystal length was 12 mm in OPA 1. When the crystal length in OPA 1 was 10 mm, the maximum measured energy was 39 mJ with M^2 = 2.9. The simulated results show a lower idler output energy then what was measured. This might be because some of the parameters in the simulations were wrong. It is also a possibility that the output signal energy from the OPA 1, which was used a pump in OPA 2, was incorrectly measured. The output signal energy from the 12 mm OPA 1 was measured to be 80.1 mJ in the position of the OPA 2 with the use of a negative uncoated CaF_2 lens for expanding the beam to reduce the fluence on the energy meter. If the absorption in this lens was higher than what was accounted for, the input pump energy in the simulations was lower than in the measurements. A second proposition for why the energies were lower in the simulations is that the diameter of the beams was smaller than estimated. When implementing the system, it was assumed that the waist of the signal and idler was in the position of the crystal inside the OPO. The relay telescope transformed the beams in this position to the position of the OPA 1 crystal (see Fig. 4.1). However, if the waist was in a position somewhere after the OPO, the relay-transformed waist could have been closer to the OPA 2 position than OPA 1 position. The beam diameters would then be bigger in the OPA 1 position and smaller in the OPA 2 position than expected. This could explain why the simulated energies were higher than the measured energies in the OPA 1 results and lower in the OPA 2 results.

Table 5.3: Measured performance parameters of OPA2. L_1 and L_2 are the crystal lengths of OPA 1 and OPA 1. E_s^{in} is the pump beam at 2.76 µm.

	L_1 [mm]	L_2 [mm]	E_s^{in}[mJ]	E_i^{in} [mJ]	E_i^{out} [mJ]	M^2
Signal and idler as seeds in OPA 1	10	5	66.2	25.3	39.0	2.9
	12	5	80.1	30.2	45.0	3.1
Signal only as seed in OPA 1	10	5	53.0	19.5	34.0	2.6
	12	5	64.1	25.0	34.0	-

Measurements of OPA 1 were also performed when only signal was used as seed in OPA 1. Table 5.3 gives an overview of the results. The near field and far field fluence distributions of the idler after OPA 2 when seeding with both signal and idler in OPA 1 can be seen in Fig. 5.11. M^2 was in general higher in the OPA 2 measurements than in the OPA 1 measurements. This is in agreement with the simulations in Fig. 3.10, which shows that M^2 increases after OPA 2 if the crystal

length is longer than 3 mm.

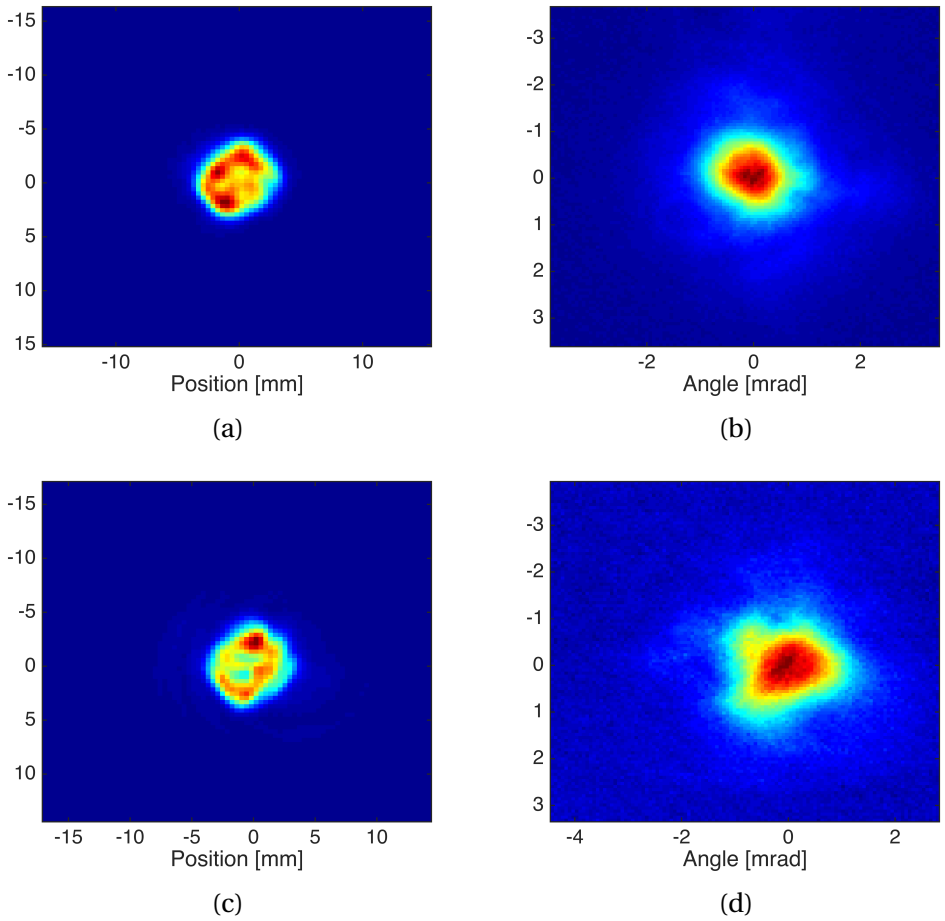

Figure 5.11: (a) and (b) shows the measured near field and far field of the 8 µm idler output from OPA 2 when the crystal length of OPA 1 was 10 mm. (d) and (c) shows the corresponding near- and far fields for the 12 mm OPA 1. Both signal and idler were used as seeds in OPA 1.

During the last experiments, a damage occurred on the 8 mm crystal used in OPA 1. The reason for this damage was the same as for the damage of the 10 mm crystal; Two damages of two new mirrors in the pump path were damaged and formed hot spots in the pump beam profile. The estimated peak fluence on the mirrors when the pump energy was 360 mJ was 1 J/cm^2. This means that the mirrors had a damage threshold lower than 1 J/cm^2, and were not suited for this experiment. The experiments was terminated after the crystal damage was observed and the beam quality was not measured for OPA 2 when the 12 mm OPA 1 was used and seeding with only signal. It is uncertain whether the damage had already occurred in the beam quality

measurement with both signal and idler as seeds. If that was the case, the beam quality could have been affected.

5.4 Summary and Further Discussion

The performances of the MOPA systems are summarized in Table 5.4. MOPA 1 and MOPA 2 are referred to the MOPAs where the crystal length in OPA 1 was 10 mm and 12 mm, respectively.

Table 5.4: Performance parameters of the two different MOPAs. The pump energy at 2.05 µm was 360 mJ.

	Signal and idler as seeds in OPA 1		Signal only as seed in OPA 1	
	MOPA 1	MOPA 2	MOPA1	MOPA 2
Crystal length OPA 1 [mm]	10	12	10	12
Crystal length OPA 2 [mm]	5	5	5	5
8 µm output energy [mJ]	39	45	34	37
Beam quality [M^2]	2.9	3.1	2.6	-

Beam quality is in general difficult to measure accurately. Many factors, such as noise in images, damages on filters and dispersion may have had an impact on the M^2 measurements. The beams went through several optical elements, such as mirrors, lenses, polarizers and filters before the near field and far field images were taken, which may have disturbed the beams. A explained in Section 4.3.4, the lens with focal length f_2 was moved to find the position of the far field. This was rather difficult to achieve with good accuracy because the estimated beam radius showed on the camera program jumped between values with large deviations.

A way to improve the experimental setup is first of all to use mirrors in the pump path with higher damage threshold. This is important in order to avoid disruptions in the beam which can result in damages on the crystals. As could be seen in Fig. 5.8, the 4 mm crystal disturbed the fluence distribution of the beams. Crystals with defects like this should be avoided as they can reduce the performance of the system. It would also have been more convenient to use only one crystal with length 12 mm instead of a combination of a 4 mm and an 8 mm crystal. This is because the coating on the crystals absorbs some of the energy. An experimental challenge during the experiments was the water vapor absorption of the signal beam, which caused an

energy loss of at least 32% when the beam propagated from the OPO to OPA 1. A solution to this problem would be to build a box around the path and flush the system with nitrogen. Another configuration to boost the energy at 8 µm even further could be to implement a third OPA 3. This OPA could be placed after OPA 1 and use the idler and pump output from OPA 1 as input beams. An illustration of the configuration can be seen in Fig. 5.12. The signal output from OPA 1 would then have to separated from the idler beam and a new path for the signal wave would have to be made so the signal beam could be used as a pump beam in OPA 2. No simulations for this experimental setup were performed, but according to theory, the idler input energy in OPA 2 would be higher with OPA 3 present, resulting in a higher idler output energy from OPA 2.

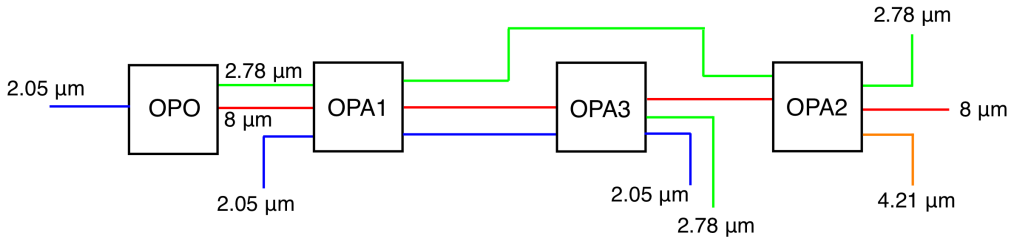

Figure 5.12: A MOPA configuration with a third stage OPA 3 inserted behind OPA 1.

A second approach, which also would resolve the problems with air absorption of the signal beam, is to only use the idler as seed in OPA 1. The idler beam at 8 µm is not near any absorption lines in the atmosphere, and the air humidity would then not affect the system. In this case, the output signal energy from the OPO will not be used, and the OPO should be optimized only to give as high as possible idler energy. A new simulation where the OPO resonator was singly resonant for the idler instead of the signal was performed. For a pump energy of 30 mJ, a beam diameter of 2.5 mm and a crystal length of 10 mm, the simulated output idler energy was 3.4 mJ with $M^2 = 2.7$. The peak fluence was 1.17 J/cm^2. Fig. 5.13 shows the simulated OPA 1 (type II) output energies when only the 3.4 mJ idler beam was used as input and the pump energy was 360 mJ.

This result shows approximately the same results as when both signal and idler were used as seeds and the OPO resonator was singly resonant for signal (Fig. 3.9a). However, the experimental result would perhaps agree more with the simulated results because the idler seed en-

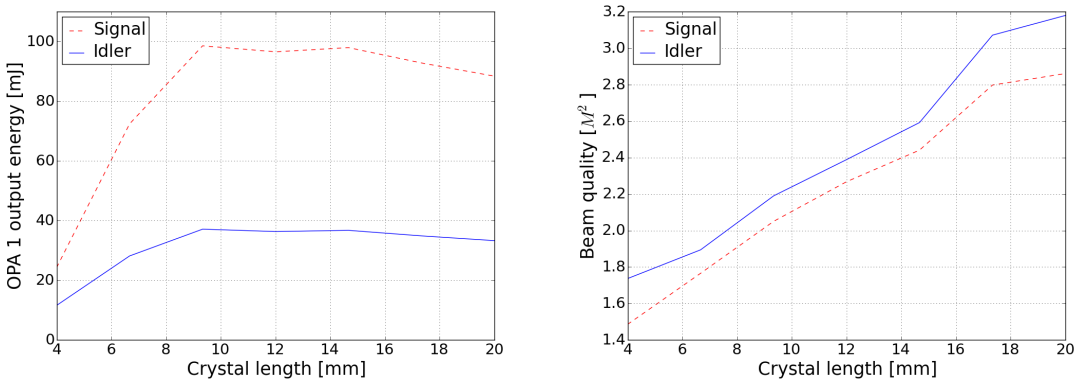

(a) (b)

Figure 5.13: Simulated OPA 1 (type II) output energy, (a), and beam quality, (b), for different crystal lengths in the first OPA stage when seeding with 3.4 mJ idler. The pump energy was 360 mJ.

ergy in the OPA 1 position would be more predictable than when seeding with signal. Seeding with only the idler beam would also resolve the alignment difficulties that can affect the wave vector mismatch.

Chapter 6

Conclusion

Conversion of laser pulses at 2.05 μm to 8 μm has been demonstrated with a ZGP master oscillator/power amplifier based on a V-shaped 3-mirror ring OPO and two OPAs. The goal of the assignment was to obtain a pulse energy of ~ 50 mJ at 8 μm wavelength, with reasonably good beam quality. The system was tested with different combinations of crystal lengths, and with both signal and idler as seeds, and only signal as seed in the power amplifier system. With a pump energy of 360 mJ, the highest pulse energy achieved at 8 μm was 45 mJ with a corresponding beam quality of $M^2 = 3.1$. This is about 4.5 times higher pulse energy than comparable existing laser sources. It was found that the beam quality generally was better when seeding with only the signal beam at 2.76 μm in the first OPA stage. It was also seen that seeding with both signal and idler did not notable increase the conversion efficiency.

An experimental challenge during the experiments was the air absorption of the signal beam, which caused a loss of energy when the beams were propagating from the OPO to the OPA. A solution to this problem would be to build a closed box flushed with nitrogen. Alignment difficulties related with dispersion of the signal and idler beams when they were propagating through lenses, were also experienced. Seeding with only one beam could resolve some of these problems. Simulations showed that a possibility is to use an OPO resonator which is singly resonant for idler, and use only the generated idler beam as seed in the OPA system.

Appendix A

Instrumentation

Mirrors:

- M_1 (OPO): QTF, 45°, HT 2.05 µm (p), HR 2.6-2.8 µm (s), HT 7.5-8.5 µm (p) (KS14014)
- M_2 (OPO): Laseroptik, 45°, HT 2.096 µm (p), HR 2.8-3.3 µm (s), HT 8.0-8.4 µm (p) (KS04039)
- M_{out} (OPO): QTF, 0°, HR 2.05 µm, R=50±5% 2.6-2.8 µm , HT 7.5-8.5 µm (KS14021)
- $M7$, $M8$: Thorlabs PF10-03-P01. Protected silver
- $M2$: HR 2.05 µm , HT 1.94 µm, 45° AOI s-pol, S2: AR@1940 s-pol (KS11011)
- $M3$, $M4$, $M5$, $M9$, $M10$: QTF, 0°, HR 2.05 µm, HT 2.6-2.8 µm, HT 7.5-8.5 µm (KS14018/19)

Wave retarders:

- $H1$, $H2$, $H3$: TwinStar, $\lambda/2$@2050nm (KB1101)

Lenses:

- $L1$: Casix, CaF_2, f=30 cm (AR-coated@2050nm)
- $L2$: Comb. of Casix, CaF_2, f=50 cm and Casix,CaF_2, f=15 cm (AR-coated@2050nm)
- $L3$: Thorlabs, CaF_2, f=10 cm, uncoated
- $L4$: Comb. of Thorlabs, CaF_2, f=75 cm, uncoated and Casix, CaF_2, f=100 cm, uncoated

Polarizers:

- $P1$, $P2$: Thin film polarizer (KP13002)

Crystals:

- OPO: BAE systems, ZGP 12x14x10 mm, $\theta = 63°$, $\phi = 45°$, AR-coating@ 2.05, 2.7-3.1, 7.5-8.5 μm, type II (KI15007)
- OPA1 (L=10mm): BAE systems, ZGP 12x14x10 mm, $\theta = 63°$, $\phi = 45°$, $\phi = 45°$, AR-coating@2.05, 2.7-3.1, 7.5-8.5 μm , type II (KI15004)
- OPA1 (L=12mm): BAE systems, ZGP 12x14x8 mm + ZGP 12x14x4 mm, $\theta = 63°$, $\phi = 45°$, AR-coating@2.05, 2.7-3.1, 7.5-8.5 μm , type II (KI15006 + KI15003)
- OPA2: BAE systems, ZGP 12x14x5 mm, $\theta = 50°$, $\phi = 0°$, AR-coating@2.05, 2.7-3.1, 7.5-8.5 μm , type I (KI15002)

Camera:

- Spiricon Inc, Pyro.electrical camera, Model: PY-III-C-B

Measuring equipment:

- Energy meter
- Spectrometer
- Oscilloscope
- Diode-detectors
- FTIR specrometer
- Filters
- Brewster stack polarizer

Appendix B

ABCD-matrix analysis

ABCD-matrix analysis is a type of ray tracing technique used to describe an optical system. The paraxial approximation is always required for ABCD matrix calculations, which means that the angular displacements θ are assumed to be small. The ray tracing technique is based on two reference planes, called the *object* and *image* planes, each perpendicular to the optical axis z of the system. The ray vector $\mathbf{r}_1$ at the given object plane $z = z_1$ can be characterized by two parameters, namely, its radial displacement x_1 from the z-axis and its angular displacement θ_1. Likewise the ray vector $\mathbf{r}_2$ at the given image plane $z = z_2$ can be characterized by x_2 and θ_2. The output and input parameters are related by the expression

$$\begin{pmatrix} x_2 \\ \theta_2 \end{pmatrix} = \begin{pmatrix} A & B \\ C & D \end{pmatrix} \begin{pmatrix} x_1 \\ \theta_1 \end{pmatrix} = \mathbf{M} \begin{pmatrix} x_1 \\ \theta_1 \end{pmatrix} \tag{B.1}$$

The ABCD-matrix $\mathbf{M}$ is a characteristic of each optical element. Propagation through free space over a distance d is associated with the matrix

$$\begin{pmatrix} 1 & d \\ 0 & 1 \end{pmatrix}, \tag{B.2}$$

and a thin lens with focal length f has the matrix

$$\begin{pmatrix} 1 & 0 \\ -1/f & 1 \end{pmatrix}. \tag{B.3}$$

Once the matrices of the elementary optical elements of a system are known, one can obtain the overall matrix by multiplying the individual matrices. For the imaging telescopes in Figs. 2.8 and 2.9, the ABCD-matrix will be

$$\mathbf{M} = \begin{pmatrix} 1 & d_3 \\ 0 & 1 \end{pmatrix} \begin{pmatrix} 1 & 0 \\ -1/f_2 & 1 \end{pmatrix} \begin{pmatrix} 1 & d_2 \\ 0 & 1 \end{pmatrix} \begin{pmatrix} 1 & 0 \\ 1/f_1 & 1 \end{pmatrix} \begin{pmatrix} 1 & d_1 \\ 0 & 1 \end{pmatrix}. \tag{B.4}$$

For the relay-imaging telescope, we have $d_1 = f_1$, $d_2 = f_1 + f_2$ and $d_3 = f_2$, and the matrix can then be written

$$M_R = \begin{pmatrix} -\frac{f_2}{f_1} & 0 \\ 0 & -\frac{f_1}{f_2} \end{pmatrix}. \tag{B.5}$$

For the Galilean imaging telescope, where $d_2 = f_1 + f_2$ the matrix will be

$$\mathbf{M}_G = \begin{pmatrix} -\frac{f_2}{f_1} & f_1 + f_2 - \frac{d_1 f_2}{f_1} - \frac{d_3 f_1}{f_2} \\ 0 & -\frac{f_1}{f_2} \end{pmatrix}. \tag{B.6}$$

The relation between the image and object plane can be found by setting element B in Eq. B.6 equal zero. It is then found that for an arbitrary image plane in position d_3, the object plane is in position

$$d_1 = \frac{f_1}{f_2}\left(f_1 + f_2 - \frac{d_3 f_1}{f_2}\right). \tag{B.7}$$

It is often necessary to combine lenses in order to obtain specific focal lengths. The combination focal length of a combination of two lenses with focal lengths f_1 and f_2 is given by

$$f = \frac{f_1 f_2}{f_1 + f_2 - d}, \tag{B.8}$$

where d is the distance between the lenses.

Appendix C

Transmission characteristics of mirrors

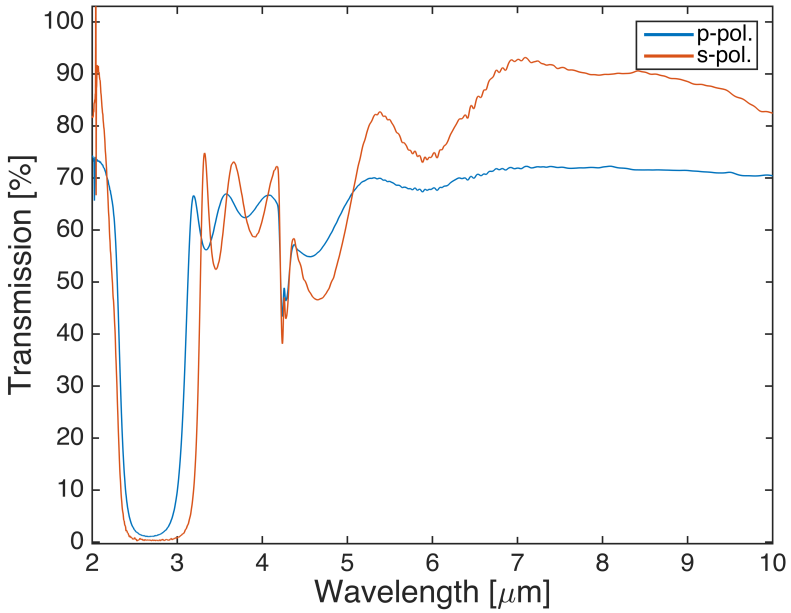

Figure C.1: Measured transmission spectrum of mirror M_1 in Fig. 4.2 (OPO in-coupling mirror). The angle of incidence was 45°.

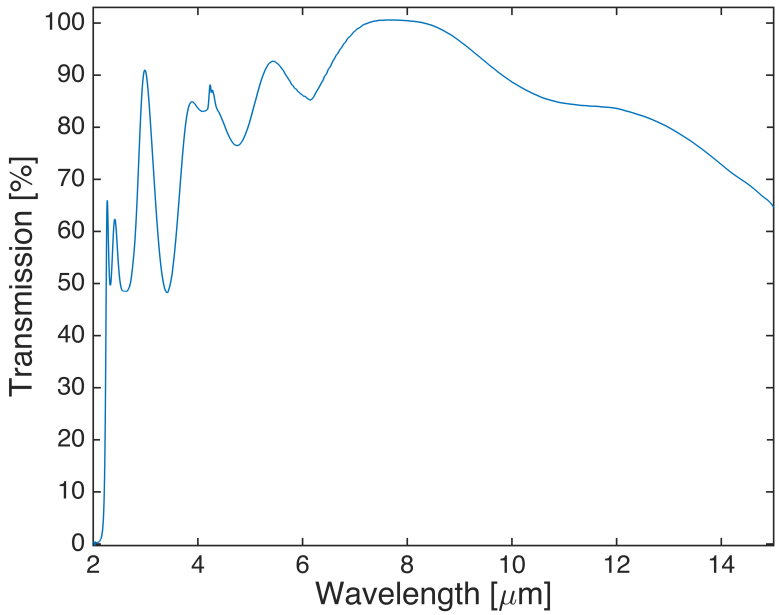

Figure C.2: Measured transmission spectrum of M_{out} in Fig. 4.2 (OPO out-coupler). The angle of incidence was 0 °.

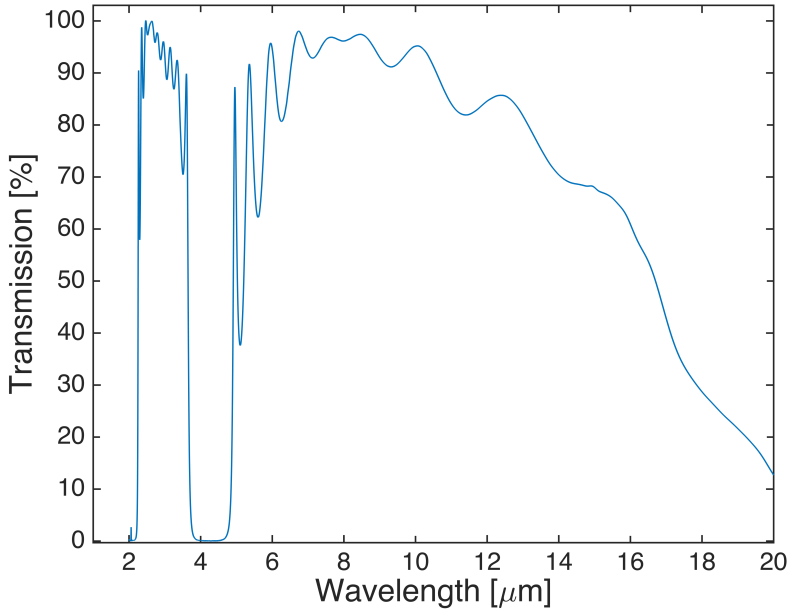

Figure C.3: Measured transmission spectrum of the mirrors $M3$, $M4$, $M5$, $M9$ and $M10$ in Fig. 4.1. The angle of incidence was 0 °.

Appendix D

Photographs of the implementation

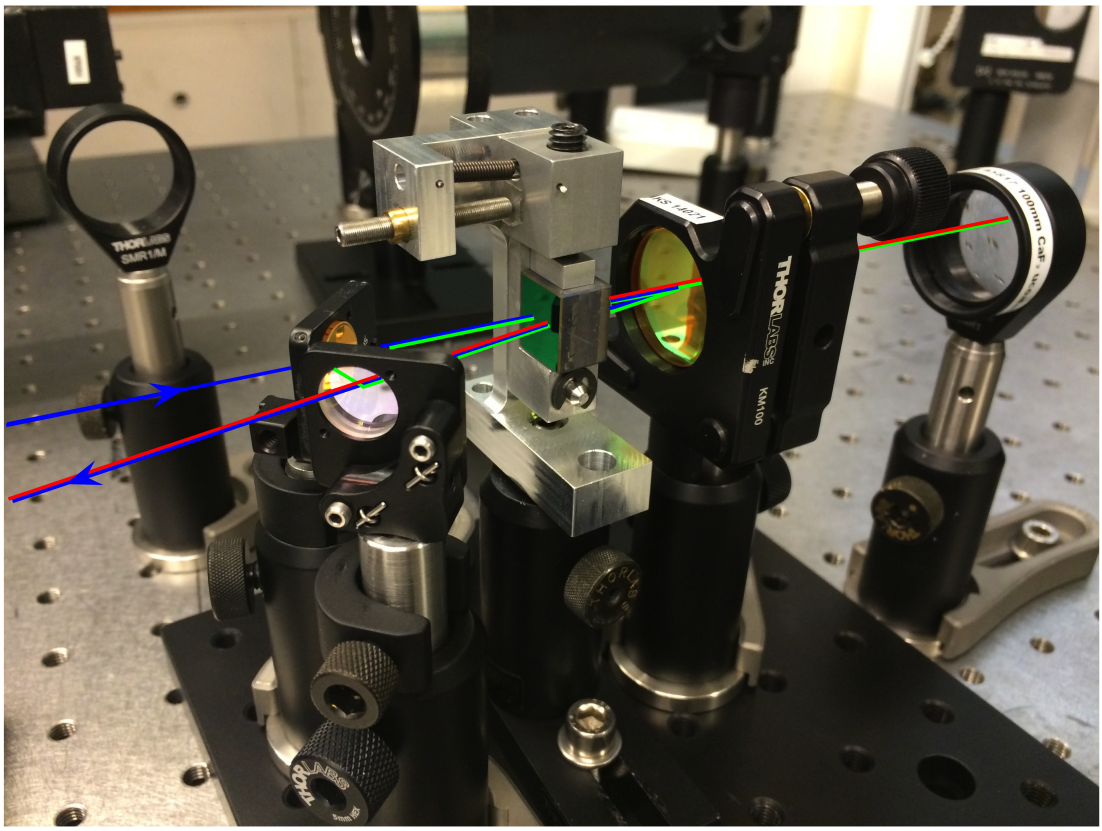

Figure D.1: The OPO configuration. The blue line is the pump path, the green line is the signal path and the red line is the idler path.

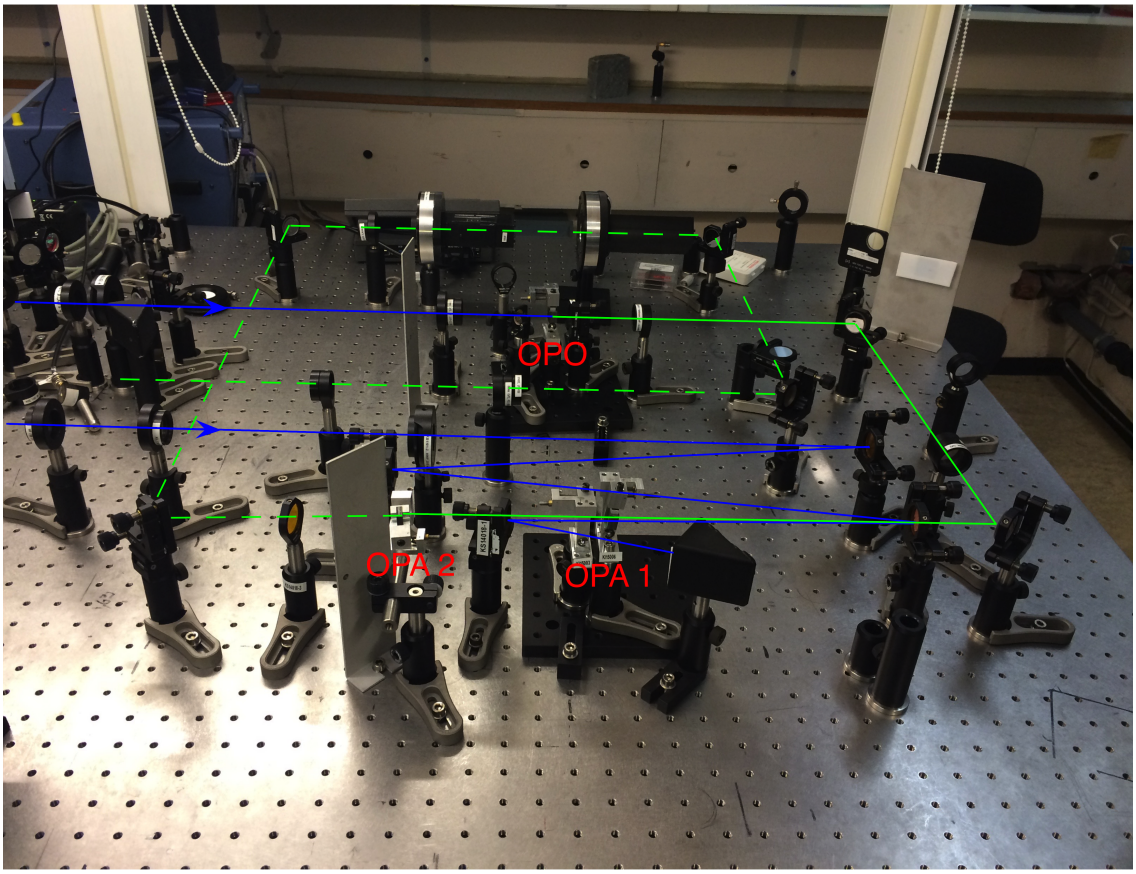

Figure D.2: The MOPA configuration. The blue line denotes the pump path and the green line denotes the signal/idler path. The green dashed path after OPA 2 was made for beam quality and energy measurements.

Appendix E

Conference Paper

We here enclose a conference paper describing the
OPO that has been accepted for presentation
at Mid-Infrared Coherent Sources (MICS).

Optical parametric oscillator at 8 μm with high pulse energy and good beam quality

Helge Fonnum, Anette Bakkland, and Magnus W. Haakestad.
FFI (Norwegian Defense Research Establishment), P.O.Box 25, NO-2027 Kjeller, Norway
Author e-mail address: Helge.Fonnum@ffi.no

Abstract: 1.8 mJ pulse energy at 8 μm is demonstrated from a $ZnGeP_2$-based optical parametric oscillator with V-shaped ring resonator, pumped with a Ho:YLF laser. The 8 μm output has a beam quality of $M^2 = 2.6$.
OCIS codes: 140.3070, 190.4410

1. Introduction

Applications of high brightness sources in the 3 – 12 μm mid-IR spectral range include spectroscopy, remote sensing, material processing, military counter measures, and surgery. Many of these applications require compact sources with good beam quality and high average power and/or high pulse energy. The mid-IR spectral band can be reached by direct laser sources, such as gas lasers, lead-salt lasers, Fe:ZnSe lasers, and quantum cascade lasers. An alternative technique is non-linear conversion of 1 μm or 2 μm laser sources. For 2 μm conversion, zinc germanium phosphide (ZGP) has become one of the preferred non-linear materials, due to its high transmission from 2 – 9 μm, high non-linearity, relatively high damage threshold, and large thermal conductivity. A challenge with optical conversion in high energy optical parametric oscillators (OPO) is that the beam diameter must be large to avoid optical damage, while at the same time the oscillator length must be kept short for small build-up time and efficient conversion. The result is a resonator with high Fresnel-number and poor beam quality. Strategies to circumvent this problem include using an unstable-resonator design with graded-reflectance output-coupler mirror (GRM), combining narrow acceptance angle phase matching with an image rotating resonator [1], or using a master-oscillator power-amplifier (MOPA) architecture [2]. In a MOPA setup, an OPO is pumped with a low-energy, narrow pump beam to maintain good beam quality. The OPO beam is then expanded and amplified in an optical parametric amplifier (OPA) where the beam quality is not degraded by the large beam size. Here we present an 8-μm-idler OPO that will be part of a ZGP-based MOPA [3], pumped with a 2.05 μm cryogenically cooled Ho:YLF laser.

2. Experiments

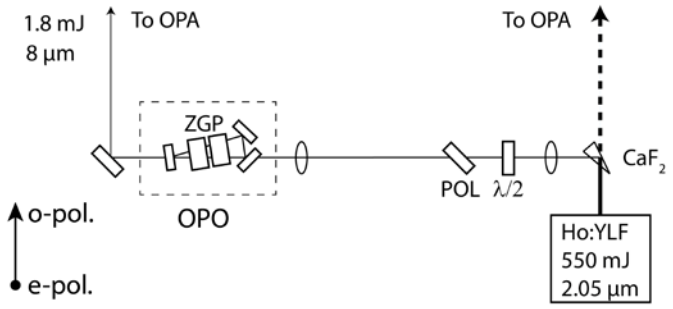

Fig. 1 Schematic of the experimental setup. A V-shaped ring OPO is pumped with 24 mJ picked off from a 550 mJ 2.05 μm cryogenic Ho:YLF laser. The OPO output and the remaining pump will be combined in an OPA. POL: polarizer, λ/2: half-wave plate.

A schematic of the experimental setup is given in Fig. 1. The Ho:YLF laser provides 550 mJ at 2.05 μm in a 14 ns pulse (FWHM), with a repetition rate of 1 Hz and a beam quality of $M^2 = 1.5$ [4]. 35 mJ of the pump is picked off by a CaF_2 wedge and can be attenuated with a wave plate and polarizer, before it is relay imaged onto the OPO with a 2.3 mm $FWe^{-2}M$ diameter. The remaining pump is to be combined with the OPO output in an OPA stage.

The OPO has a V-shaped three-mirror ring resonator allowing for double-pass pumping in the same crystal, without overlapping forward and backward propagating beams. The benefits compared to a linear resonator are elimination of feedback into the pump laser, and reduced fluence at the ZGP crystal. The OPO output coupler reflects 50% of

the signal beam (2.8 µm), while it has high reflectance for the pump (2.05 µm) and high transmittance for the idler (8 µm). The other two resonator mirrors have high transmittance for the p-polarized pump and idler, and high reflectance for the s-polarized signal. A high idler out-coupling at all resonator mirrors helps improving the beam quality, because it minimizes back-conversion. The physical perimeter of the ring is 130 mm. The ZGP crystal is manufactured by BAE systems, and is AR coated for the pump, signal and idler. It is cut at $\theta = 63°$, $\varphi = 45°$ for type II phase matching, and angle tuned to provide a signal and idler wavelength of 2.76 µm and 8.0 µm, respectively. The crystal length is 10 mm, and the aperture is 12 mm x 14 mm. To avoid damage, the pump fluence is limited to 1.4 J/cm^2, which gives a maximum pump energy of 24 mJ. Figure 1 shows measured output energy and spectrum from the OPO. The maximum total output energy (signal + idler) is 8.1 mJ, of which 1.8 mJ is at 8 µm. Figure 2 shows the measured near field and far field idler beam profiles. The beam quality of the idler is $M^2 = 2.6$ at maximum output energy.

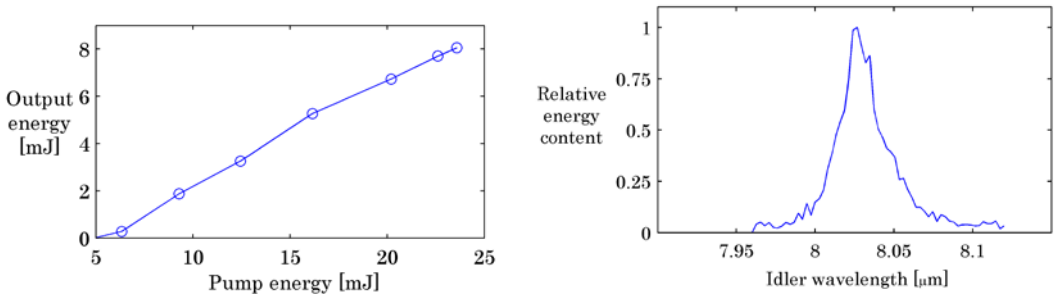

Fig. 2. Left: Measured output energy (signal + idler) from the OPO. Right: Measured idler spectrum.

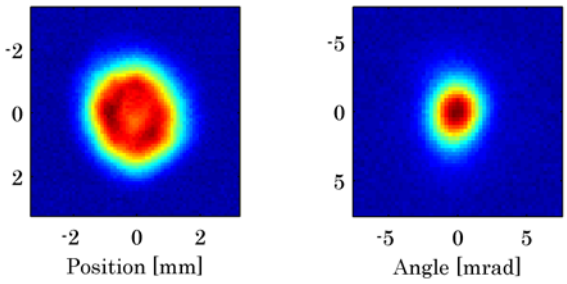

Fig. 3. Measured near field (left) and far field (right) of the 8 µm idler output from the OPO.

4. Conclusion

In summary, we have demonstrated 1.8 mJ at 8 µm from a V-shaped ZGP ring OPO with beam quality 2.6. The OPO is the implementation of the first stage in a MOPA setup with a potential for good-beam-quality, several tens-of-mJ output at 8 µm.

References

1. Smith and M. S. Bowers, "Image-rotating cavity designs for improved beam quality in nanosecond optical parametric oscillators," JOSA B **18**, 706-713 (2001).

2. M. W Haakestad et al., "Mid-infrared source with 0.2 J pulse energy based on nonlinear conversion of Q-switched pulses in $ZnGeP_2$," Optics Express **22**, 8556-8564 (2014).

3. E. Lippert et al., "Laser source with high pulse energy at 3 – 5 µm and 8 – 12 µm based on nonlinear conversion in $ZnGeP_2$ (invited paper)," in SPIE Security + Defence, Amsterdam, paper no. 9251-13 (2014).

4. H. Fonnum et al., "550 mJ Q-switched cryogenic Ho:YLF oscillator pumped with a 100 W Tm:fiber laser," Optics Letters **38**, 1884-1886 (2013).

Bibliography

[1] Helge Fonnum, Anette Bakkland, and Magnus W. Haakestad. Optical parametric oscillator at 8 μm with high pulse energy and good beam quality. *Mid-Infrared Coherent Sources (MICS)*, Long Beach, CA, USA, Mar. 2015.

[2] Dr. Irina T. Sorokina and Dr. Konstantin L. Vodopyanov. Solid-state mid-infrared laser sources. *Topics in Applied Physics*, 89, 2003.

[3] J. A. Giordmaine and Robert C. Miller. Tunable coherent parametric oscillation in $LiNbO_3$ at optical frequencies. *Phys. Rev. Lett.*, 14:973–976, Jun 1965.

[4] Antoine Godard. Infrared (2–12 μm) solid-state laser sources: A review. *Comptes Rendus Physique*, 8:1100–1128, Des 2007.

[5] Magnus W. Haakestad, Helge Fonnum, and Espen Lippert. Mid-infrared source with 0.2 J pulse energy based on nonlinear conversion of Q-switched pulses in $ZnGeP_2$. *Opt. Express*, 22(7):8556–8564, Apr 2014.

[6] Helge Fonnum, Espen Lippert, and Magnus W. Haakestad. 550 mJ Q-switched cryogenic Ho:YLF oscillator pumped with a 100 W Tm:fiber laser. *Optics Letters*, 38:1884–1886, Apr 2013.

[7] Gabriel Mennerat and Philippe Kupecek. High-energy narrow-linewidth tunable source in the mid infrared. In *Advanced Solid State Lasers*, page FC13. Optical Society of America, 1998.

[8] Y. Ehrlich, S. Pearl, , and S. Fastig. High brightness tunable tandem optical parametric oscillator at 8-12 μm. *Advanced Solid-State Photonics*, 2004.

[9] Magnus W. Haakestad, Gunnar Arisholm, Espen Lippert, Stephane Nicolas, Gunnar Rustad, and Knut Stenersen. High-pulse-energy mid-infrared lasersource based on optical parametric amplification in $ZnGeP_2$. *Opt. Express*, 16(18):14263–14273, Sep 2008.

[10] Robert W. Boyd. *Nonlinear Optics*. Academic Press, 2003.

[11] J. E. Midwinter and J. Warner. The effects of phase matching method and of uniaxial crystal symmetry on the polar distribution of second-order non-linear optical polarization. *British Journal of Applied Physics*, 16(8):1135, 1965.

[12] A. V. Smith, D. J. Armstrong, and W. J. Alford. Increased acceptance bandwidths in optical frequency conversion by use of multiple walk-off-compensating nonlinear crystals. *Opt. Soc. Am. B*, 15:4335–4340, Jan 1998.

[13] N. Boeuf, D. Branning, I. Chaperot, E. Dauler, S. Guérin, G. Jaeger, A. Muller, and A. Migdall. Calculating characteristics of non-collinear phase-matching in uniaxial and biaxial crystals. *Optical Engineering*, 39(4):1016–1024, 2000.

[14] A. E. Siegman. Defining, measuring, and optimizing laser beam quality. *Proc. SPIE*, 1868: 2–12, 1993.

[15] ISO 11146-2:2005. Lasers and laser-related equipment - test methods for laser beam widths, divergence angles and beam propagation ratios - part 2: General astigmatic beams. (18), 2007.

[16] A. V. Smith and M. S. Bowers. Image-rotating cavity designs for improved beam quality in nanosecond optical parametric oscillators. *J. Opt. Soc. Am. B*, 18:706–713, 2001.

[17] Alexey Dergachev, Darrell Armstrong, Arlee Smith, Thomas Drake, and Marc Dubois. High-power, high-energy ZGP OPA pumped by a 2.05- µm Ho:YLF MOPA system. *Nonlinear Frequency Generation and Conversion: Materials, Devices, and Applications VI*, 6875, 2008.

[18] URL www.inradoptics.com/pdfs/Inrad_WP_ZGP.pdf.

[19] Subhasis Das, Gopal C. Bhar, Sudipto Gangopadhyay, and Chittaranjan Ghosh. Linear and nonlinear optical properties of $ZnGeP_2$ crystal for infrared laser device applications: revisited. *Appl. Opt.*, 42(21):4335–4340, Jul 2003.

[20] Espen Lippert, Helge Fonnum, and Magnus W. Haakestad. Laser source with high pulse energy at 3-5 μm and 8-12 μm based on nonlinear conversion in $ZnGeP_2$. *Proc. SPIE*, 9251, 2014.

[21] Espen Lippert, Helge Fonnum, Gunnar Arisholm, and Knut Stenersen. A 22-watt mid-infrared optical parametric oscillator with V-shaped 3-mirror ring resonator. *Opt. Express*, 18(25):26475–26483, Dec 2010.